



# Elucidating the structural evolution of highly efficient Co–Fe bimetallic catalysts for the hydrogenation of CO<sub>2</sub> into olefins

Na Liu<sup>a,b</sup>, Jian Wei<sup>a,\*</sup>, Jing Xu<sup>a,b</sup>, Yang Yu<sup>a,b</sup>, Jiafeng Yu<sup>a</sup>, Yu Han<sup>a,b</sup>, Kai Wang<sup>a,b</sup>, Joshua Iseoluwa Orege<sup>a,b</sup>, Qingjie Ge<sup>a,\*</sup>, Jian Sun<sup>a</sup>

<sup>a</sup> Dalian National Laboratory for Clean Energy, Dalian Institute of Chemical Physics, Chinese Academy of Sciences, Dalian 116023, China

<sup>b</sup> University of Chinese Academy of Sciences, Beijing 100049, China

## ARTICLE INFO

### Keywords:

CO<sub>2</sub> hydrogenation  
Cobalt-iron alloy carbide  
Structural evolution  
Proximity  
Olefin synthesis

## ABSTRACT

Constructing Co-Fe bimetallic catalyst is of high research value for CO<sub>2</sub> conversion based on its outstanding traits, however, its activity-structure relationship is still confusing. Herein, a series of Na-promoted Co-Fe bimetallic catalysts differing in composition or proximity were prepared and their structural evolution during reduction and reaction was elucidated. It was found that the Co<sub>1</sub>Fe<sub>2</sub> catalyst with Co/Fe molar ratio of 1/2 and close proximity was conducive to rapid reduction of CoFe<sub>2</sub>O<sub>4</sub> to Co<sub>x</sub>Fe<sub>y</sub> alloy, and further carbonization to stable  $\chi$ -(Co<sub>x</sub>Fe<sub>1-x</sub>)<sub>5</sub>C<sub>2</sub> alloy carbide as the active phase for olefin formation, thus exhibiting superior performance without evident deactivation for over 500 h on-stream. Especially at high space velocity, it achieved an unprecedented olefin space-time yield up to 1810.8 mg·g<sub>cat</sub><sup>-1</sup>·h<sup>-1</sup>, showing a potential application in micro-channel reactor. Moreover, the alloy carbide plays a unique role in facilitating CO<sub>2</sub> adsorption, and inhibiting the hydrogenation of surface intermediates as well as suppressing carbon deposition.

## 1. Introduction

Directly converting CO<sub>2</sub> into high-value chemicals provides an attractive approach for addressing the dual challenges of energy crisis and climate change [1]. Among them, selective production of olefins has a bright prospect for industrialization. Olefins as particularly important industrial feedstocks for other chemicals (e.g., plastics, fibers) can be produced directly from CO<sub>2</sub> hydrogenation by Fischer-Tropsch synthesis (FTS) or methanol-mediated (MeOH) routes [2,3]. CO<sub>2</sub>-FTS route can be divided into two successive reactions: (i) first convert CO<sub>2</sub> into CO via the reverse water gas shift (RWGS) reaction and then (ii) hydrogenate CO to C<sub>2+</sub> hydrocarbons via FTS reaction. Fe-based catalysts have been widely studied for CO<sub>2</sub>-FTS route due to their high activity for both above reactions [4–7]. Co-based catalysts, as another industrial and commercial catalysts, have been extensively explored in CO hydrogenation as the latter reaction of CO<sub>2</sub>-FTS, showing high selectivity for long chain hydrocarbons at relatively low temperature [8]. However, focusing on the CO<sub>2</sub> hydrogenation reaction over Co-based catalysts, the product is mainly CH<sub>4</sub> with less C<sub>2+</sub> hydrocarbons [9–12]. The significant difference in product selectivity between Fe- and Co-based catalysts in CO<sub>2</sub> hydrogenation can be explained mainly by the lack of RWGS

activity over Co-based catalysts [13]. As two traditional industrial catalysts used in CO<sub>2</sub> hydrogenation, Fe-based catalysts are considered as higher selectivity for olefins with inexpensive cost, but less activity [14, 15]. In contrast, Co-based catalysts has higher activity and reducibility, but are limited by the ability of further hydrogenation to CH<sub>4</sub> [16]. Therefore, the construction of cobalt-iron bimetallic catalysts with both high activity and reducibility of cobalt as well as high selectivity to olefins of iron is currently desired for CO<sub>2</sub> hydrogenation.

Up to now, many efforts have been dedicated to exploring the advantages of cobalt-iron bimetallic catalysts for CO<sub>2</sub> hydrogenation, but the distinctions of active phase between cobalt-iron bimetallic catalysts and traditional Fe- or Co-based catalysts remain puzzling, let alone the elucidation of the detailed structural evolution process. Previous studies have found that the addition of alkaline metals (such as Na and K) is conducive to the adsorption and activation of CO<sub>2</sub>, and plays an essential role in accelerating the structural evolution of Fe-based catalysts to form iron carbide phase ( $\chi$ -Fe<sub>5</sub>C<sub>2</sub>) [6,17]. A small addition of K can dramatically enhance the formation of olefins on cobalt-iron bimetallic catalysts [18]. In addition, many studies have focused on the proximity of Fe and Co in the catalyst precursors, such as cobalt-iron oxalate [13,19], cobalt-iron oxide [20,21] and layered double hydroxide [22–25], to

\* Corresponding authors.

E-mail addresses: [weijian@dicp.ac.cn](mailto:weijian@dicp.ac.cn) (J. Wei), [geqj@dicp.ac.cn](mailto:geqj@dicp.ac.cn) (Q. Ge).

<https://doi.org/10.1016/j.apcatb.2023.122476>

Received 16 December 2022; Received in revised form 6 February 2023; Accepted 15 February 2023

Available online 16 February 2023

0926-3373/© 2023 Elsevier B.V. All rights reserved.

improve the selectivity of target products. However, it is still difficult to make sure whether the proximity, especially in the active phases, is remained during CO<sub>2</sub> hydrogenation [26,27]. Co element in cobalt-iron bimetallic catalysts can promote the consumption of CO produced in the RWGS reaction and are strongly associated with the formation of carbides during CO<sub>2</sub> hydrogenation reaction [28]. This can be simply described that Co involves in the formation of iron carbides, specifically Co insertion into the lattice of  $\chi$ -Fe<sub>5</sub>C<sub>2</sub>, replacing the Fe position [29,30]. However, how the composition and proximity of Co and Fe in the precursors of cobalt-iron bimetallic catalysts affect the formation and evolution of active phase during CO<sub>2</sub> hydrogenation remains a mystery.

In present work, we prepared a series of Na-modified mono- and bimetallic catalysts with different Co/Fe molar ratios and compared the catalytic performance of CoFe catalysts with various proximity prepared by different method for selective synthesis of olefins from CO<sub>2</sub> hydrogenation. The structural evolution, adsorption and surface reactivity behavior of the catalysts were investigated by a variety of advanced characterization techniques. we found that the composition and proximity of Co and Fe in catalysts could reveal the intrinsic relationship between the structural evolution and olefin synthesis during CO<sub>2</sub> hydrogenation. The Co1Fe2 catalyst with the sole CoFe<sub>2</sub>O<sub>4</sub> spinel structure in precursor exhibited more excellent ability of rapid reduction and carbonization evolving from originally CoFe<sub>2</sub>O<sub>4</sub> to Co<sub>x</sub>Fe<sub>y</sub> alloy and finally to  $\chi$ -(Co<sub>x</sub>Fe<sub>1-x</sub>)<sub>5</sub>C<sub>2</sub>. Consequently, it presented more distinguished catalytic performance than other catalysts studied without obvious deactivation during 500 h stability test. This work was expected to provide a helpful consideration for studying the structural evolution of cobalt-iron bimetallic catalysts.

## 2. Experimental section

### 2.1. Catalyst preparation

Co-Fe bimetallic catalysts were prepared by a co-precipitation method followed by hydrothermal treatment in term of the reported procedures [31,32]. Typically, Co(NO<sub>3</sub>)<sub>2</sub>·6H<sub>2</sub>O and Fe(NO<sub>3</sub>)<sub>3</sub>·9H<sub>2</sub>O with different Co/Fe ratios were dissolved sequentially in 75 mL of deionized water ([Co]<sup>2+</sup> + [Fe]<sup>3+</sup> = 0.09 M) with continuous stirring. Subsequently, 5 mol·L<sup>-1</sup> of NaOH aqueous solution was dropped into above solution under constantly stirring at 60 °C until the pH reached at 11, and then the stirring was continuously kept for 1 h. The precipitated hydroxides were subsequently transferred to two 100 mL Teflon lined autoclaves and placed in a static oven at 150 °C for 24 h. After being centrifuged and washed with 400 mL of deionized water, the solid phase product was dried at 80 °C for 12 h. Finally, the obtained was calcined in a muffle furnace at 400 °C for 3 h. The final products with Co/Fe molar ratio = 1/4, 1/2, 1/1, 2/1, 4/1 were denoted as Co1Fe4, Co1Fe2, Co1Fe1, Co2Fe1 and Co4Fe1, respectively, based on the molar ratio Co to Fe in raw materials. Furthermore, monometallic Co1 and Fe1 samples were synthesized following a similar procedure, whereas using only Co (NO<sub>3</sub>)<sub>2</sub>·6H<sub>2</sub>O or Fe(NO<sub>3</sub>)<sub>3</sub>·9H<sub>2</sub>O, respectively. In order to explore the effect of Na promoter, Co1Fe2-Na-free catalyst was prepared by a similar procedure, using a solution of 10 wt% NH<sub>4</sub>OH as precipitant.

The phy-Co1Fe2 sample was synthesized by directly mixing powder of above Co1 and Fe1 catalysts with a molar ratio of Co/Fe = 1/2 in an agate mortar for 1 min. In addition, the im-Co1Fe2 sample was synthesized by impregnation method. Typically, the aqueous solution of Co (NO<sub>3</sub>)<sub>2</sub>·6H<sub>2</sub>O was impregnated on Fe1 catalyst with a molar ratio of Co/Fe = 1/2. Subsequently, the sample was rested at room temperature for 10 h and then dried at 80 °C for 12 h before being calcined at 400 °C for 3 h.

### 2.2. Catalyst characterization

In order to investigate the contents of Na promoter, the inductively coupled plasma optical emission spectrometer (ICP-OES) were detected

on PerkinElmer 7300 DV instrument over the calcined catalysts. X-ray photoelectron spectroscopy (XPS) analysis was conducted on a Thermo Fischer ESCALAB 250XI instrument by using Al-K $\alpha$  X-ray radiation source (Passing energy: 30 eV; hv: 1486.6 eV). The spectrograms at different depths were carried out by sputtering with 2 kV Ar<sup>+</sup> for corresponding time on calcined and spent catalysts. The deconvolution of XPS spectra was performed using the Thermo Advantage program with Gaussian function by subtracting smart peak background, using the C 1 s peak at 284.8 eV to calibrate the binding energy of the detected elements. The X-ray Diffraction (XRD) measurements of the catalysts were performed on a PANalytical X'Pert Pro diffractometer with Cu-K $\alpha$  radiation source ( $\lambda$  = 1.5 Å, 40 kV, 40 mA). *In situ* XRD measurements were collected on an Empyrean-100 PANalytical diffractometer with Cu-K $\alpha$  radiation ( $\lambda$  = 1.5 Å, 40 kV, 40 mA), including two atmosphere operation processes under atmospheric pressure. The reduction process was carried out from room temperature heated up to 350 °C (heating rate: 5 °C·min<sup>-1</sup>) and then maintained at 350 °C for a period in 50%H<sub>2</sub>/50% N<sub>2</sub> stream. After cooling to 320 °C naturally, the feed gas with H<sub>2</sub>/CO<sub>2</sub> = 3 was simultaneously injected into the system and maintained, which was called reaction process. The <sup>57</sup>Fe Mössbauer spectroscopy (MES) technique was performed on spent catalysts to detect Fe species, using a Topologic 500 A spectrometer under room temperature with <sup>57</sup>Co (Rh) as irradiation source. The transmission electron microscopy (TEM) and element mapping images were collected by a Talos F200X G2 instrument (Acceleration voltage: 200 kV). X-ray absorption spectroscopy (XAS) data at the K-edge were carried out recorded at room temperature in transmission mode on the BL14W beamline of Shanghai Synchrotron Radiation Facility (SSRF) in China.

All temperature programmed experiments were performed on MICROTRAC MRB BELCAT II equipment with the catalysts loaded on a quartz reactor. In H<sub>2</sub>-temperature programmed reduction (H<sub>2</sub>-TPR) experiments, the H<sub>2</sub> signals were recorded with a thermal conductivity detector (TCD). Firstly, 40 mg of calcined catalysts were pretreated at 300 °C for 60 min in pure Ar flow. After cooling to 50 °C, a steady 5%H<sub>2</sub>/95%Ar flow was injected to the quartz reactor with the temperature heated to 900 °C at a heating rate of 10 °C·min<sup>-1</sup>. In temperature programmed hydrogenation (TPH) experiments, 80 mg of spent catalysts were pretreated at 300 °C for 120 min in pure He flow. After cooling to 50 °C, the catalysts were exposed to pure H<sub>2</sub> flow with the temperature increasing from 50 °C to 900 °C (5 °C·min<sup>-1</sup>), during which H<sub>2</sub>O ( $m/z$  = 18) and CH<sub>4</sub> ( $m/z$  = 16) signals were monitored. C<sub>3</sub>H<sub>6</sub>-pulse transient hydrogenation experiments were performed on spent catalysts. Prior to the pulse experiments, 50 mg of the samples were pretreated at 350 °C for 120 min in pure H<sub>2</sub> stream to reduce the passivated surface. After cooling to 50 °C, the samples were followingly exposed on pure H<sub>2</sub> stream. During 5%C<sub>3</sub>H<sub>6</sub>/95%Ar pulsed into pure H<sub>2</sub> system, the information of C<sub>3</sub>H<sub>6</sub> ( $m/z$  = 42), C<sub>3</sub>H<sub>8</sub> ( $m/z$  = 44) and CH<sub>4</sub> ( $m/z$  = 16) as transient response signal for were obtained by a mass spectrometer. In temperature programmed desorption (CO<sub>2</sub>-TPD or CO-TPD) experiments, prior to the adsorption, 100 mg of reduced catalysts were pretreated at 350 °C for 120 min in pure H<sub>2</sub> flow to reduce the passivated surface. After cooling to 50 °C, the gas was switched to 5%CO<sub>2</sub>/95%He (CO<sub>2</sub>-TPD) or 5%CO/95%He (CO-TPD) for 30 min for saturated adsorption, then to pure He flow for 30 min to flush physisorbed CO<sub>2</sub> or CO. Subsequently, a pure He flow was injected with the temperature reaching up to 900 °C with a heating rate of 10 °C·min<sup>-1</sup>, during which CO ( $m/z$  = 28) and CO<sub>2</sub> ( $m/z$  = 44) signals were detected by a mass spectrometer.

*In situ* high pressure diffuse reflectance infrared Fourier transform spectroscopy (DRIFTS) was carried on PerkinElmer Frontier. The samples were reduced in pure H<sub>2</sub> flow at 350 °C for 2 h and then flushed in Ar flow for 1 h. After the *in situ* cell was cooled down to 320 °C, the feed gas flow (H<sub>2</sub>/CO<sub>2</sub> = 3) was injected to increase the reaction pressure to 2.0 MPa and maintain for 1.5 h, during which the spectrum was collected.

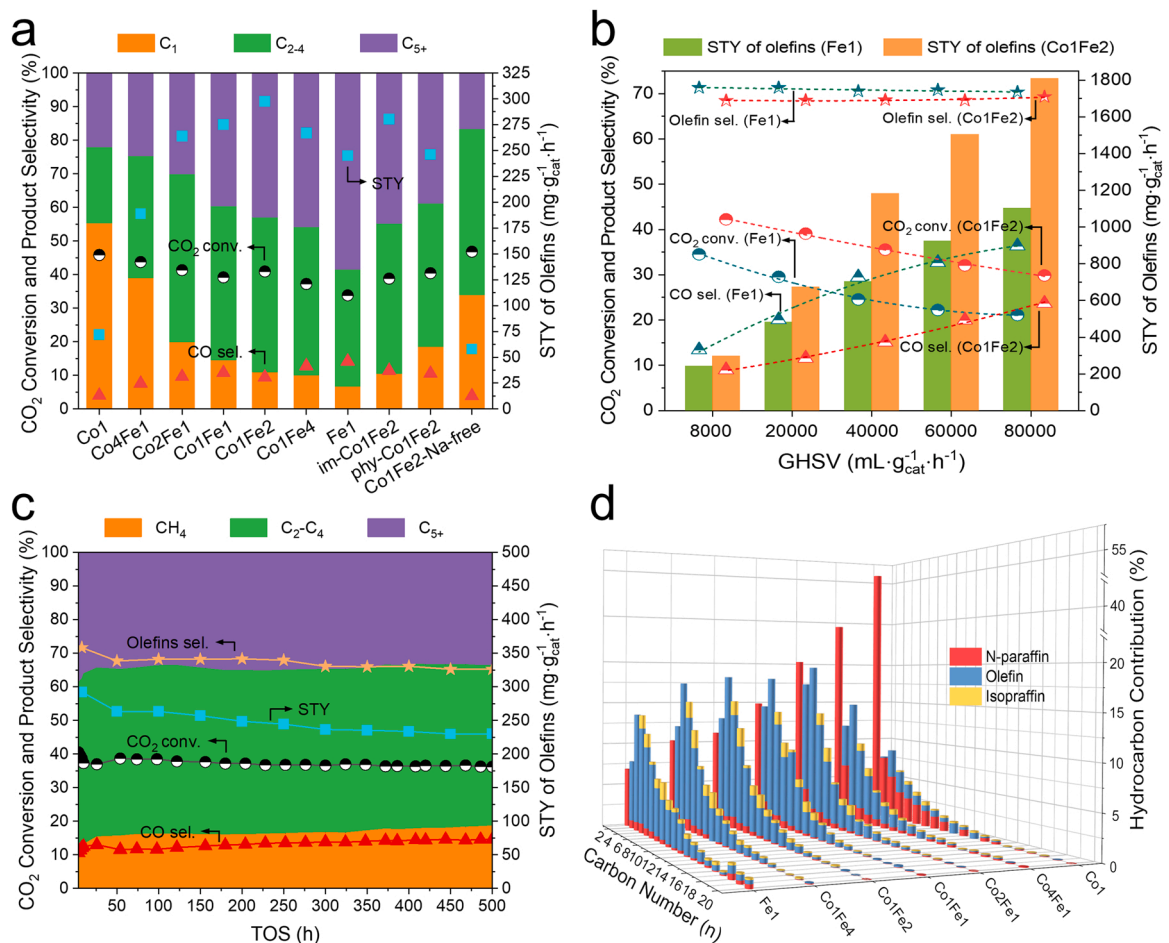


**Fig. 1.** Catalytic performances of the catalysts. a) Catalytic performances of all catalysts studied with TOS of 8 h. b) Catalytic performances of Fe1 and Co1Fe2 catalysts at different GHSV conditions. c) Catalytic activity and product selectivity of Co1Fe2 catalyst within 500 h stability test. d) Product distribution (C-mol%) of a series of catalysts with different Co/Fe ratios. Reaction conditions:  $\text{H}_2/\text{CO}_2 = 3$ ,  $320^\circ\text{C}$ , 2 MPa,  $8000\text{ mL}\cdot\text{g}_{\text{cat}}^{-1}\cdot\text{h}^{-1}$  (for a, c, d), and  $80000\text{--}8000\text{ mL}\cdot\text{g}_{\text{cat}}^{-1}\cdot\text{h}^{-1}$  (for b).

### 2.3. Catalyst activity test

Catalytic performance test was conducted in a traditional stainless steel fixed-bed reactor. Unless otherwise stated, the catalytic performances of different catalysts were investigated and compared under the conditions of  $\text{GHSV} = 8000\text{ mL}\cdot\text{g}_{\text{cat}}^{-1}\cdot\text{h}^{-1}$ ,  $T = 320^\circ\text{C}$ ,  $P = 2\text{ MPa}$ ,  $\text{H}_2/\text{CO}_2 = 3$ . To be specific, the calcined catalyst was *in situ* reduced in pure  $\text{H}_2$  flow at  $350^\circ\text{C}$  for 8 h under atmospheric pressure. Then the temperature was decreased to  $320^\circ\text{C}$  (naturally cooling), the mixture gas ( $\text{H}_2/\text{CO}_2/\text{N}_2 = 72/24/4$ , where the  $\text{N}_2$  act as the internal standard) was injected to the reactor with the system pressure increased to 2 MPa for catalyst evaluation. In addition, the space velocity exploration tests were carried out on the calcined Co1Fe2 and Fe1 catalysts varying GHSV from 80000 to  $8000\text{ mL}\cdot\text{g}_{\text{cat}}^{-1}\cdot\text{h}^{-1}$  with other reaction conditions same as above. During the reaction, the organic products were detected by an online Agilent 7890B instrument with a flame ionization detector (FID) with a capillary column of PONA type. The organic products were cooled and remained in a cold trap. Subsequently, the gas products ( $\text{CO}$ ,  $\text{CH}_4$ ,  $\text{N}_2$  and  $\text{CO}_2$ ) were analyzed on an online thermal conductivity detector (TCD, GC-2014AT, SHIMADZU) using a TDX-01 column. Furthermore, the condensation of products was prevented by heating the pipelines between the reactor and GC at  $180^\circ\text{C}$ .

Herein,  $\text{CO}_2$  conversion, CO selectivity and the hydrocarbon distribution (not counting CO product) were calculated as following Eqs. (1–3).

$$\text{CO}_2 \text{ conversion } (\%) = \frac{\text{CO}_{2 \text{ in}} - \text{CO}_{2 \text{ out}}}{\text{CO}_{2 \text{ in}}} \times 100\% \quad (1)$$

$$\text{CO selectivity } (\%) = \frac{\text{CO}_{\text{out}}}{\text{CO}_{2 \text{ in}} - \text{CO}_{2 \text{ out}}} \times 100\% \quad (2)$$

$$C_i \text{ hydrocarbon selectivity (C - mol\%)} = \frac{\text{mol of } C_i \text{ hydrocarbon} \times i}{\sum_i \text{mol of } C_i \text{ hydrocarbon} \times i} \times 100\% \quad (3)$$

where the  $\text{CO}_{\text{out}}$  represents the mole of CO in the outlet, and  $\text{CO}_{2 \text{ in}}$  and  $\text{CO}_{2 \text{ out}}$  represent the moles of  $\text{CO}_2$  in the inlet and outlet, respectively.

## 3. Results and discussion

### 3.1. Catalytic performance of catalysts during $\text{CO}_2$ hydrogenation

The  $\text{CO}_2$  hydrogenation performances of a series of cobalt and iron monometallic (Co1, Fe1) or bimetallic (Co1Fe4, Co1Fe2, Co1Fe1, Co2Fe1 and Co4Fe1) catalysts prepared by precipitation method, which were subsequently collectively referred to as “catalysts with different Co/Fe ratio”, as well as physically mixed (phy-Co1Fe2) and impregnated (im-Co1Fe2) catalysts were obtained under the conditions of  $T = 320^\circ\text{C}$ ,  $P = 2\text{ MPa}$ ,  $\text{GHSV} = 8000\text{ mL}\cdot\text{g}_{\text{cat}}^{-1}\cdot\text{h}^{-1}$ ,  $\text{H}_2/\text{CO}_2 = 3$ . The catalytic performance at time on stream of 8 h ( $\text{TOS} = 8\text{ h}$ ) is shown in

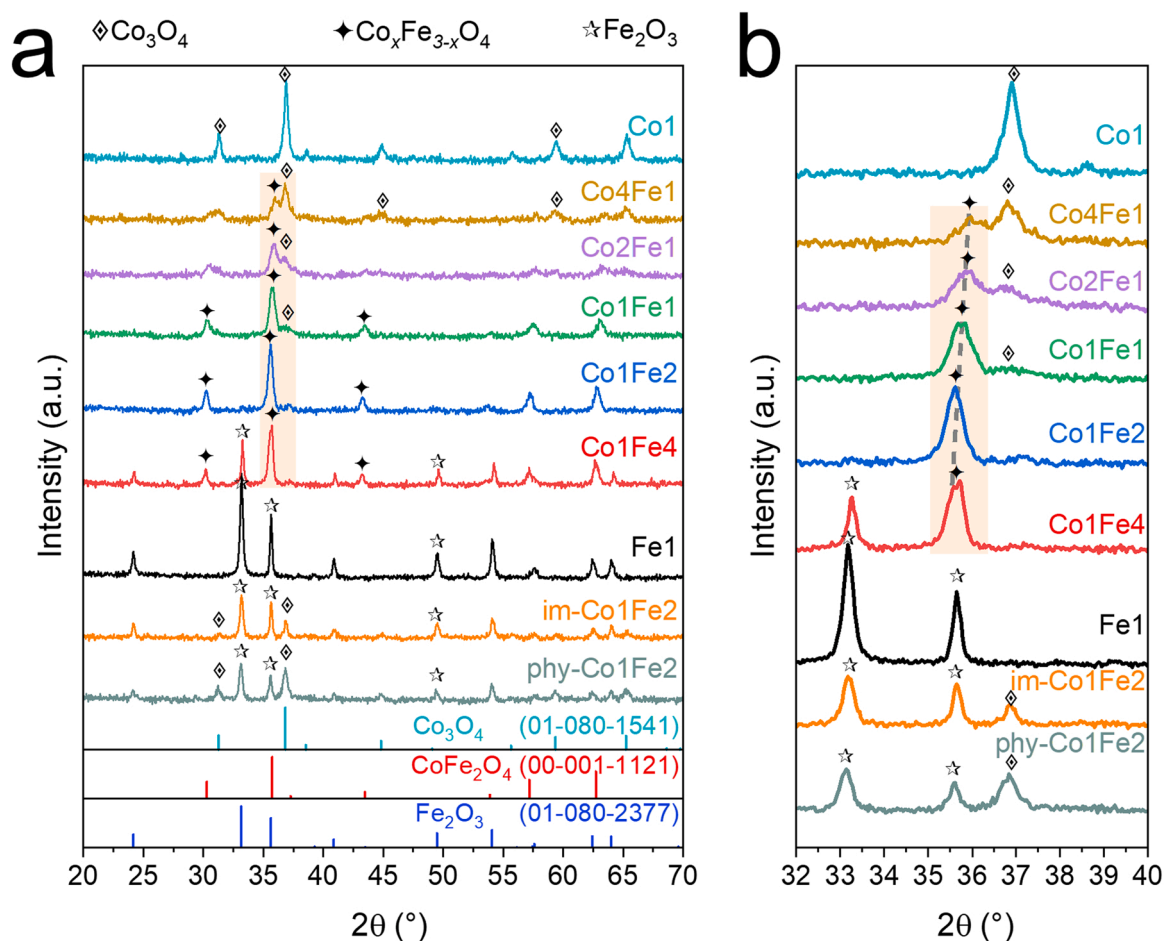


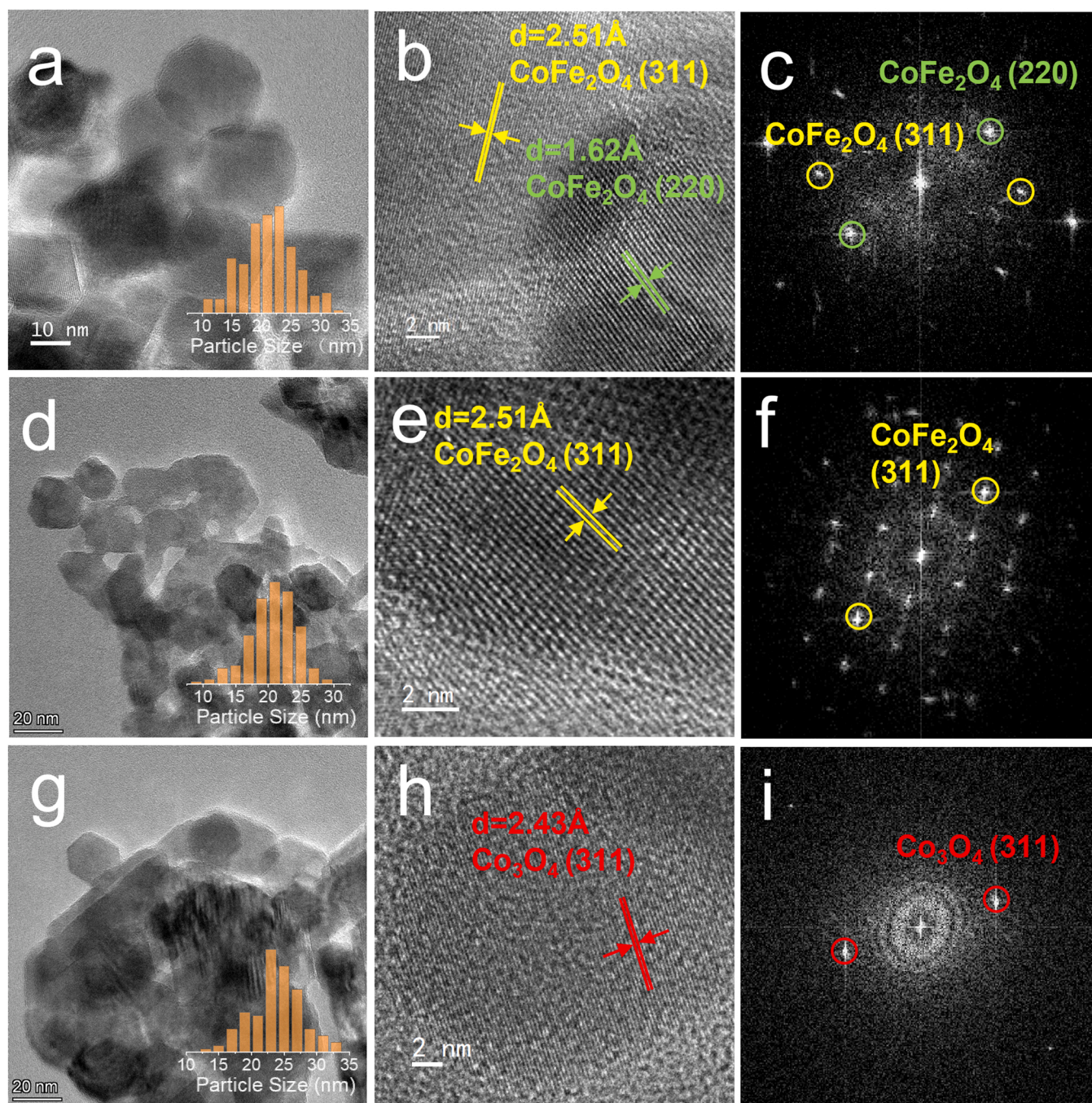
Fig. 2. XRD patterns of calcined catalysts with  $2\theta = 20^\circ - 70^\circ$  and  $2\theta = 32^\circ - 40^\circ$ .

Fig. 1a and Table S1. Some clear trends in the performance of the catalysts with different Co/Fe ratios are that as the molar ratio of Co/Fe decreases in the corresponding precursor,  $\text{CO}_2$  conversion decreases from 45.8% (for Co1 catalyst) to 33.8% (for Fe1 catalyst) with CO selectivity increasing from 4.0% to 14.2%, accompanied by a marked decrease in  $\text{CH}_4$  selectivity from 55.3% to 6.8% in hydrocarbon products. Furthermore, the selectivity of  $\text{C}_{2+}$  olefins in hydrocarbon products increases from 13.7% (for Co1 catalyst) to 74.3% (for Fe1 catalyst). It is notably that when the molar ratio of Co/Fe is less than or equal to 1 (Co1Fe4, Co1Fe2 and Co1Fe1 catalysts), the olefin selectivity is higher than 70% for all the catalysts. It is worth emphasizing that, as the molar ratio of Co/Fe decreases, the space time yield (STY) of  $\text{C}_{2+}$  olefins present a distinct volcanic-type distribution, achieving the maximum over Co1Fe2 catalyst, which first rises from 72.0 (for Co1 catalyst) to 297.4 (for Co1Fe2 catalyst) then decreases to 245.0 (for Fe1 catalyst)  $\text{mg} \cdot \text{g}_{\text{cat}}^{-1} \cdot \text{h}^{-1}$ . In the GHSV exploration experiments (Fig. 1b and Table S2), with adjusting the GHSV from 8000 to 80000  $\text{mL} \cdot \text{g}_{\text{cat}}^{-1} \cdot \text{h}^{-1}$ , it is observed that the  $\text{CO}_2$  conversion decreases from 42.1% to 29.9% and the CO selectivity increases from 9.0% to 23.7%, along with similar olefin selectivity of about 69% over Co1Fe2 catalyst, while the  $\text{CO}_2$  conversion over Fe1 catalyst decreases remarkably from 34.5% to 21.1% with CO selectivity increasing from 13.4% to 36.4% and a similar olefin selectivity of about 71%. To our surprise, the STY over Co1Fe2 catalyst dramatically reaches up to 1810.8  $\text{mg} \cdot \text{g}_{\text{cat}}^{-1} \cdot \text{h}^{-1}$  at GHSV of 80000  $\text{mL} \cdot \text{g}_{\text{cat}}^{-1} \cdot \text{h}^{-1}$ , which is significantly superior to that of Fe1 catalyst (1104.2  $\text{mg} \cdot \text{g}_{\text{cat}}^{-1} \cdot \text{h}^{-1}$ ) at same conditions, suggesting that Co1Fe2 catalyst is suitable for micro-channel reactor.

The above results justify that the Co1Fe2 catalyst presents relatively excellent catalytic performance compared to other catalysts with

different Co/Fe ratios, which is also at a relatively high level among reported Fe-based catalysts for olefin synthesis in literatures (Table S3). The catalytic activity and product selectivity within 500 h reaction of Co1Fe2 catalyst is plotted with a function of time on stream in Fig. 1c. It is worth mentioning that Co1Fe2 catalyst exhibits significant stability over a time on stream of 500 h. The  $\text{CO}_2$  conversion over Co1Fe2 catalyst changes slightly from 38.6% (at 50 h) to 36.2% (at 500 h), along with a gradual decrease of  $\text{C}_{2+}$  olefin selectivity in hydrocarbon products from 67.7% to 65.2%, and the corresponding STY of  $\text{C}_{2+}$  olefins drop gradually from 263.2 to 230.0  $\text{mg} \cdot \text{g}_{\text{cat}}^{-1} \cdot \text{h}^{-1}$ . Furthermore, as the molar ratio of Co/Fe increases in catalysts, the product distribution shifting to lighter hydrocarbons is observed in Fig. 1d. Considering the similar olefin selectivity over the catalysts with molar ratio of Co/Fe less than or equal to 1, this phenomenon could be described as that the construction of Co-Fe bimetallic catalysts is conducive to the concentration of carbon number distribution and the generation of light olefins without sacrificing the selectivity of total olefins. In addition, compared to phy-Co1Fe2 catalyst and im-Co1Fe2 catalyst with the same Co/Fe molar ratio of 1/2, the Co1Fe2 catalyst prepared by direct co-precipitation of Co and Fe displays higher  $\text{CO}_2$  conversion and higher total olefin selectivity, which may be related to the proximity of Co and Fe in the precursor. Moreover, compared with Co1Fe2 catalyst, Co1Fe2-Na-free catalyst is undesirably selective to paraffins with 34.0%  $\text{CH}_4$  and only 10.7%  $\text{C}_{2+}$  olefins in hydrocarbon, indicating the significant effect of Na promoter for suppressing paraffin formation and promoting carbon chain growth. [33,34] Because the Na contents are regulated to similar levels in other catalysts using NaOH as precipitant (Table S4), the influence of Na promoter is not further elaborated in this work. In summary, cobalt-iron bimetallic catalysts present multiple advantages





**Fig. 3.** TEM and HRTEM images of calcined catalysts. (a, b, c) of Co<sub>1</sub>Fe<sub>2</sub>; (d, e, f) of Co<sub>2</sub>Fe; (g, h, i) of Co<sub>1</sub>.

in catalytic activity and olefin selectivity as well as mechanical and chemical stability, which provides a promising strategy for the design of industrial catalyst for CO<sub>2</sub> hydrogenation.

### 3.2. Physicochemical properties of the calcined catalysts

As described above, a series of catalysts with different Co/Fe ratio were prepared by a precipitation method followed by hydrothermal treatment. The crystal structures of the calcined catalysts were preliminarily discussed by XRD (Fig. 2). The diffraction patterns of the calcined Fe<sub>1</sub> and Co<sub>1</sub> catalysts match with  $\alpha$ -Fe<sub>2</sub>O<sub>3</sub> (JCPDS 01–080–2377) and cubic spinel structure Co<sub>3</sub>O<sub>4</sub> (JCPDS 01–080–1541), respectively, and both crystallize well. For the Co-Fe bimetallic catalysts prepared by precipitation method, the diffraction peak at originally  $2\theta = 36.8$  and

$43.5^\circ$  attributed to the CoFe<sub>2</sub>O<sub>4</sub> (JCPDS 00–001–1121) phase shifting to the direction of  $2\theta$  increase with the increase of Co/Fe ratio is detected as shown in Fig. 2b. This phenomenon originates from that the smaller radius Co<sup>3+</sup> (0.61 Å) replaces Fe<sup>3+</sup> (0.65 Å) in the octahedral position in the Co-Fe bimetallic catalysts, causing the crystal structure to shrink and the diffraction peak to shift [35]. Therefore, the characteristic diffraction peaks at about  $36.8$  and  $43.5^\circ$  could be attributed to the Co<sub>x</sub>Fe<sub>3–x</sub>O<sub>4</sub> inverse spinel phase [36]. For Co<sub>1</sub>Fe<sub>2</sub> catalyst with a Co/Fe molar ratio of 1/2, all diffraction peaks accurately match with the standard card of CoFe<sub>2</sub>O<sub>4</sub>, identifying that the main phase of Co<sub>1</sub>Fe<sub>2</sub> catalyst is a strictly crystalline cubic spinel CoFe<sub>2</sub>O<sub>4</sub> structure. However, the Co<sub>x</sub>Fe<sub>3–x</sub>O<sub>4</sub> structure is not the single phase for other Co-Fe bimetallic catalysts with the molar ratio of Co/Fe deviating from 1/2, but also accompanied by  $\alpha$ -Fe<sub>2</sub>O<sub>3</sub> phase for Co<sub>1</sub>Fe<sub>4</sub> catalyst, or Co<sub>3</sub>O<sub>4</sub> phase for Co<sub>1</sub>Fe<sub>1</sub>, Co<sub>2</sub>Fe<sub>1</sub>

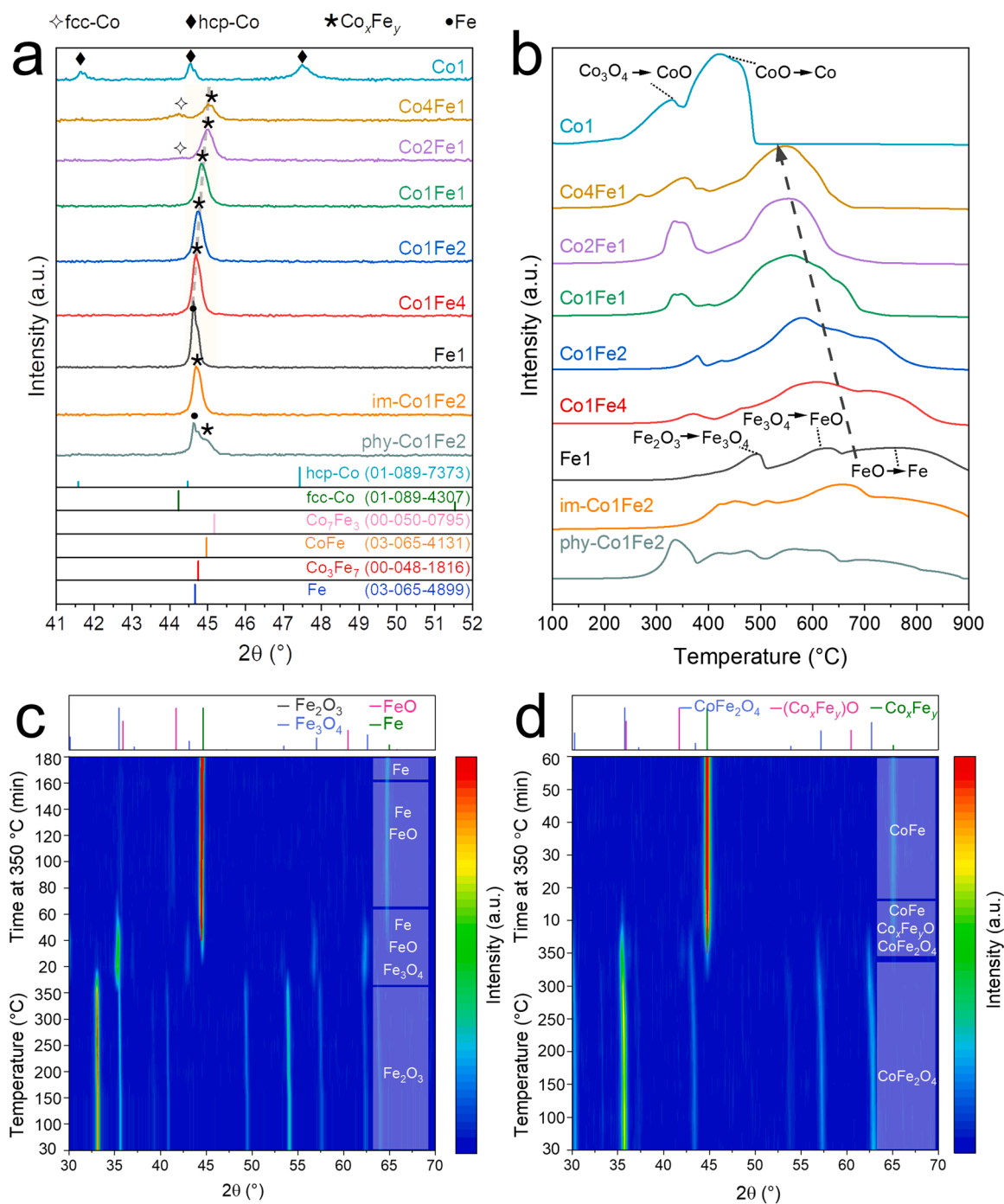


**Fig. 4.** Reduction behavior of the catalysts. a) XRD patterns of the reduced catalysts with  $2\theta = 41\text{--}52^\circ$ . Reduction conditions: 350 °C for 8 h under atmospheric pressure at pure  $\text{H}_2$  atmosphere ( $25 \text{ mL}\cdot\text{min}^{-1}$ ). b)  $\text{H}_2$ -TPR profiles of the calcined catalysts. Contour map and *in situ* XRD patterns for Fe1 (c) and Co1Fe2 (d) catalysts during reduction process.

and Co4Fe1 catalysts, respectively. In addition, for im-Co1Fe2 and phy-Co1Fe2 catalysts, there is no strong interaction between Co and Fe elements in precursor, which can be confirmed by the observation of their original phases in the XRD pattern without spinel  $\text{Co}_x\text{Fe}_{3-x}\text{O}_4$  phase. In view of the relatively superior performance co-precipitated of Co1Fe2 catalyst (Fig. 1a), it indicates that an appropriate composition and proximity of Co-Fe bimetallic catalysts are vital to the catalytic performance of olefin synthesis from  $\text{CO}_2$  hydrogenation.

In order to further probe the structure details of catalysts, TEM and HRTEM of representative Co1Fe2, Co2Fe1 and Co1 catalysts were applied as shown in Fig. 3. The morphology of Co1Fe2 and Co2Fe1

catalysts resembles a spherical ball with a diameter of 21 nm (Fig. 3a, d), different from that of the angular Co1 catalyst with a diameter of 23 nm (Fig. 3g), suggesting that the existence of Fe element has a discernible effect on the morphology of monometallic Co catalyst. The presence of interplanar spacing of 2.51 Å in the HRTEM images of Co1Fe2 (Fig. 3b, c) and Co2Fe1 (Fig. 3e, f) catalysts conforms to the (311) plane of  $\text{CoFe}_2\text{O}_4$ . The interplanar spacing of 2.43 Å of Co1 catalyst corresponds to the (311) plane of spinel  $\text{Co}_3\text{O}_4$  (Fig. 3h, i). The results of HRTEM analysis are consistent with those discussion about XRD measurement (Fig. 2). Moreover, the elemental mapping of the calcined Co1Fe2 catalyst presents that all elements (Co, Fe, Na and O) are homogeneously



dispersive represented by the corresponding colors in Fig. S1.

To further validate the relationship between chemical state and phase structure induced by the composition variation of Co and Fe, XPS experiments were conducted to probe the electronic state and near-surface component on calcined catalysts. The quantitative analysis of different surface species can be visibly summarized by deconvolution of XPS spectra, shown in Fig. S2 and Fig. S3. According to the high-resolution Fe 2p spectra (Fig. S2), the binding energies at about 709.3 eV ( $2p_{3/2}$ ) and 721.8 eV ( $2p_{1/2}$ ) are attributed to  $Fe^{2+}$  species, and the binding energies at about 711.5 eV ( $2p_{3/2}$ ) and 724.5 eV ( $2p_{1/2}$ ) are attributed to  $Fe^{3+}$  species [37]. A bright trend can be generalized as that the overall peak intensity of all Fe species gets weaker with increasing the molar ratio of Co/Fe in co-precipitated Co-Fe bimetallic catalysts, which is attributed to the decreasing of Fe content in catalyst. For the high-resolution Co 2p spectra (Fig. S3), the overall peak intensity is observed to be stronger with the increasing of the molar ratio of Co/Fe in Co-Fe bimetallic catalysts, and the broad peaks at 780.1 eV ( $2p_{3/2}$ ) and 795.3 eV ( $2p_{1/2}$ ) can be attributed to  $Co^{3+}$  species, respectively, while the peaks at 782.4 eV ( $2p_{3/2}$ ) and 797.4 eV ( $2p_{1/2}$ ) can be attributed to  $Co^{2+}$  species, respectively [38,39]. As summarized in Table S5, the chemical states of Fe and Co present +2 and +3 valence states in all Co-Fe bimetallic catalysts studied. It suggests that Co and Fe atom co-share the tetrahedral sites and the octahedral sites, verifying that the formation of an inverse spinel structure for Co-Fe bimetallic catalysts, according to the previous reports [31,40]. In addition, the proportion variation of each valence state in its element is very clear. Specifically, as the molar ratio of Co/Fe increases, the proportions of  $Fe^{2+}$  and  $Co^{3+}$  species increase, while the proportions of  $Fe^{3+}$  and  $Co^{2+}$  species decrease, proving that the octahedral site are more likely to be occupied by  $Co^{2+}$  species in the catalyst with more Co content, which further confirms the shrinkage of crystal structure. This result is consistent with XRD patterns (Fig. 2).

The textural properties of the catalysts with different Co/Fe ratios were conducted by  $N_2$  adsorption-desorption experiments, exhibited in Fig. S4 and Table S4. The  $N_2$  adsorption-desorption isotherms of all calcined catalysts exhibit typical type-IV isotherm with type-H2 hysteresis loop, suggesting that all catalysts investigated are mesoporous in nature according to the IUPAC classification [41]. Combined with the morphology and structure displayed by the TEM (Fig. 3a, d and g), we extrapolate that the porous structure is derived from the spaces between catalyst particles. As seen in Fig. S4b, all catalysts investigated exhibit a wide pore distribution, while the average pore diameter of Co-Fe bimetallic catalysts is larger than that of monometallic catalysts (Table S4). The surface area and total pore volume of the calcined catalysts take on a volcanic-type trend with the increase of Co/Fe ratio, reaching the maximum value at the calcined Co1Fe1 catalyst, which is mutually corroborated with the fact that the particle size of Co-Fe bimetallic catalysts is smaller than monometallic Co catalyst obtained from TEM (Fig. 3a, d and g), further proving the close proximity between Co and Fe in Co-Fe bimetallic catalysts. Therefore, cobalt-iron bimetallic catalysts have more potential to exhibit excellent pore environment than monometallic Co1 and Fe1 catalysts.

### 3.3. Reduction behavior of the calcined catalysts

The reduction behavior of the catalysts was characterized by *in/ex-situ* XRD and  $H_2$ -TPR, shown in Fig. 4. As shown in Fig. 4a ( $2\theta = 41\text{--}52^\circ$ ) and Fig. S5 ( $2\theta = 20\text{--}80^\circ$ ), the Fe1 catalyst can be completely converted from  $\alpha\text{-Fe}_2O_3$  to metallic Fe (JCPDS 03-065-4899) after reduction. For the co-precipitated Co-Fe bimetallic catalysts, it is observed that the strongest diffraction peak at  $2\theta = 44.6^\circ$  of the original metallic Fe shifts to higher  $2\theta$  angles with increasing Co content. After comparing with the standard card of  $Co_3Fe_7$  (JCPDS 00-048-1816), CoFe (JCPDS 03-065-4131) and  $Co_7Fe_3$  (JCPDS 00-050-0795) alloy phases where the corresponding characteristic diffraction peak obviously shifts to higher  $2\theta$  angles with increasing Co/Fe ratio in alloy phases, this

diffraction peak at about  $2\theta = 45^\circ$  of the Co-Fe bimetallic catalysts can be attributed to the  $Co_xFe_y$  alloy phase. It suggests that the molar ratio of Co/Fe in precursors is a factor of affecting the final composition of the reduced  $Co_xFe_y$  alloy phases. Furthermore, the diffraction peaks of the reduced phy-Co1Fe2 catalyst could be further assigned to metallic Fe and  $Co_xFe_y$  alloy phases, which is different from the reduced Co1Fe2 catalyst. It is also worth mentioning that the diffraction peaks of im-Co1Fe2 catalyst can be attributed to the  $Co_xFe_y$  alloy phase, while its offset of  $2\theta$  about  $2\theta = 45^\circ$  is lower than that of Co1Fe2 catalyst. It suggests that the proximity between Co and Fe in precursors has a major influence on reduction and the close proximity is conducive to the formation of  $Co_xFe_y$  alloy phase. Another interesting phenomenon is that the calcined Co1 catalyst could be completely reduced to hcp-Co phase (JCPDS 01-089-7373) at  $350^\circ\text{C}$ , consistent with the previous reports [10]. When the molar ratio of Co/Fe is more than 1/2, the structure of fcc-Co (JCPDS 01-089-4307) is detected in reduced Co2Fe1 and Co4Fe1 catalysts, manifesting that the  $Co_3O_4$  phase in the corresponding calcined catalysts is reduced to fcc-Co instead of hcp-Co, speculating that the formation of cobalt-iron bimetal is beneficial to induce the transformation of the metallic Co crystal during the reduction process [42].

*In situ* XRD experiments were performed to over Fe1 and Co1Fe2 catalysts to further track the dynamic structural evolution during the reduction process, which were shown in Figs. 4c and 4d, respectively. The Fe1 catalyst initially maintains the original  $Fe_2O_3$  phase with no remarkable change during the process of elevating temperature in 50%  $H_2$ /50% $N_2$  flow (Fig. 4c). When the temperature reaches  $350^\circ\text{C}$  and then remains constant, the Fe1 catalyst starts to be successively reduced to  $Fe_3O_4$  and FeO, and finally to metallic Fe at  $350^\circ\text{C}$  for 160 min. Comparatively, for the Co1Fe2 catalyst (Fig. 4d), all diffraction peaks attributed to the original  $CoFe_2O_4$  phase are noticed below  $350^\circ\text{C}$ . Until the reduction temperature rises to  $350^\circ\text{C}$  with a heating rate of  $5^\circ\text{C}\cdot\text{min}^{-1}$ , the diffraction peaks of  $CoFe_2O_4$  are observed to be weaker, accompanied with the appearance of diffraction peaks at  $2\theta = 36.0, 42.1$  and  $44.7^\circ$ . Among them, the diffraction peak at  $2\theta = 44.7^\circ$  belongs to the  $Co_xFe_y$  alloy phase. Considering the relationship between Co and Fe in calcined and reduced Co-Fe bimetallic catalysts, the diffraction peaks at  $2\theta = 36.0$  and  $42.1^\circ$  could be attributed to  $(Co_xFe_y)O$  oxide phase. After reduction at  $350^\circ\text{C}$  for 20 min, the diffraction peaks of  $Co_xFe_y$  alloy are detected without characteristic diffraction peaks of other phases, proving that the Co1Fe2 catalyst could be reduced to the final reducing phase in much shorter time than Fe1 catalyst. The above results indicate that the formation of Co-Fe bimetal can promote the reduction of iron species and shorten the reduction time. This view could be further demonstrated by the  $H_2$ -TPR experiments.

In  $H_2$ -TPR profiles (Fig. 4b), the Fe1 catalyst with three groups of reduction peaks at 490, 630 and  $760^\circ\text{C}$ , respectively, shows that the Fe1 catalyst evolves from the initial  $\alpha\text{-Fe}_2O_3$  through  $Fe_3O_4$ , FeO, and finally to metallic Fe [43,44]. The Co1 catalyst possesses two groups of reduction peaks, including a low temperature peak at  $325^\circ\text{C}$  and a high temperature peak at  $430^\circ\text{C}$ , which can be attributed to the reduction of the initial calcined  $Co_3O_4$  to CoO and CoO to metallic Co, respectively [45]. For Co-Fe bimetallic catalysts, the reduction behavior can be further subdivided into two stages: the reduction peak at low temperature for the initial  $Co_3O_4$  phase to CoO, and the reduction peak at high temperature for the initial  $CoFe_2O_4$  phase to  $(Co_xFe_y)O$  oxide phase and finally reduced to  $Co_xFe_y$  alloy, where the reduction behavior of  $(Co_xFe_y)O$  oxide phase is similar to the FeO phase. When the molar ratio of Co/Fe increases in catalysts, the position of the reduction peaks at high temperature obviously shifts toward the lower temperature, suggesting that the addition of Co element can improve the reduction ability of the Co-Fe bimetallic catalysts, which validates the conclusion obtained from *in situ* XRD experiments (Fig. 4c, d). In addition, by comparing the  $H_2$ -TPR curves of im-Co1Fe2, phy-Co1Fe2 and Co1Fe2 catalysts with same composition but different proximity in precursor, their reductive behavior is quite different. This remarkable change also can be reflected

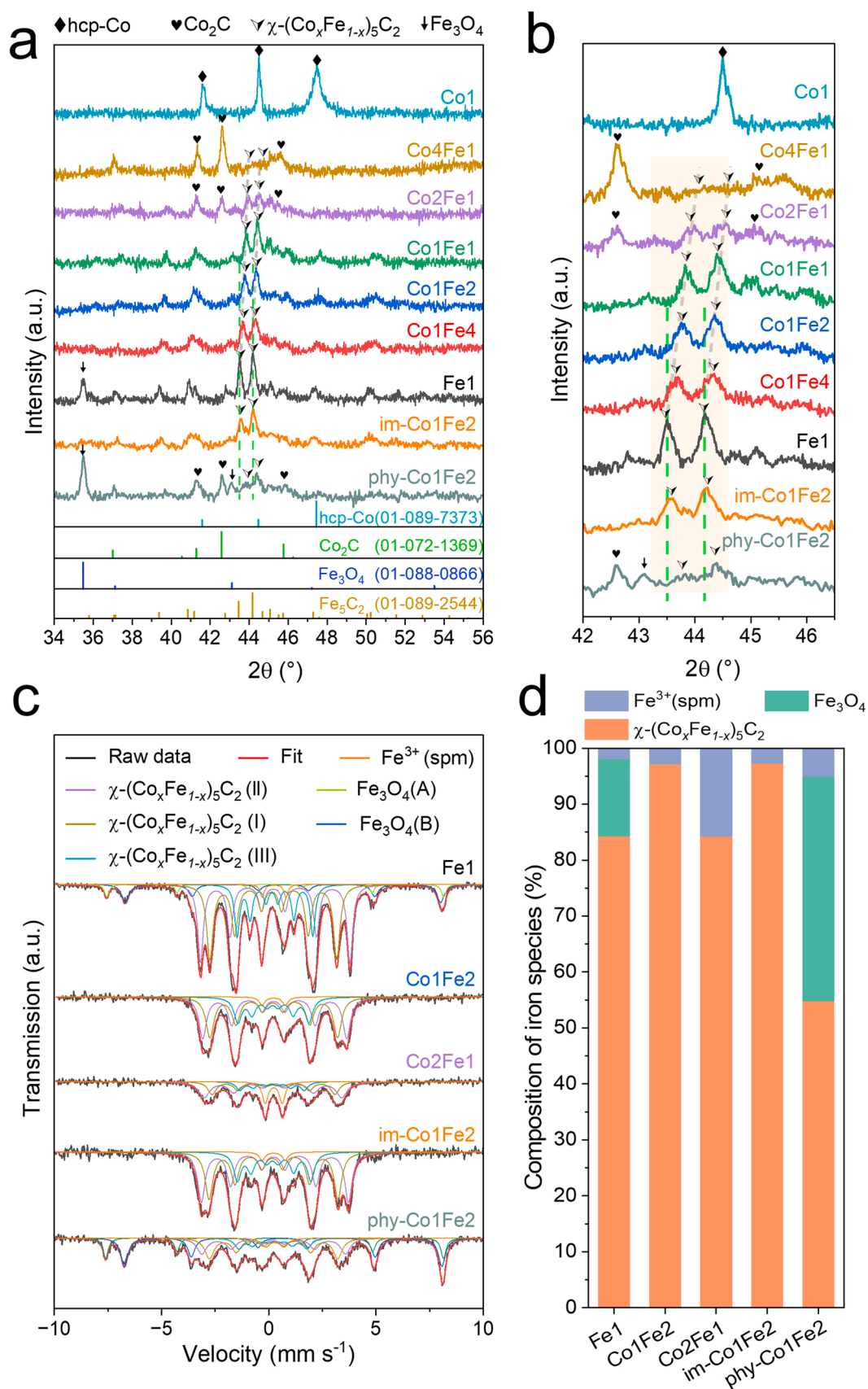


**Fig. 5.** The characterization of phase and structure for the spent catalyst. XRD patterns of the spent catalysts with  $2\theta = 34\text{--}56^\circ$  (a) and  $2\theta = 42\text{--}46.5^\circ$  (b). <sup>57</sup>Fe Mössbauer spectra (c) and the corresponding composition of iron species (d) of spent F1, Co1Fe2, Co2Fe1, im-Co1Fe2 and phy-Co1Fe2 catalysts. TOS = 24 h.



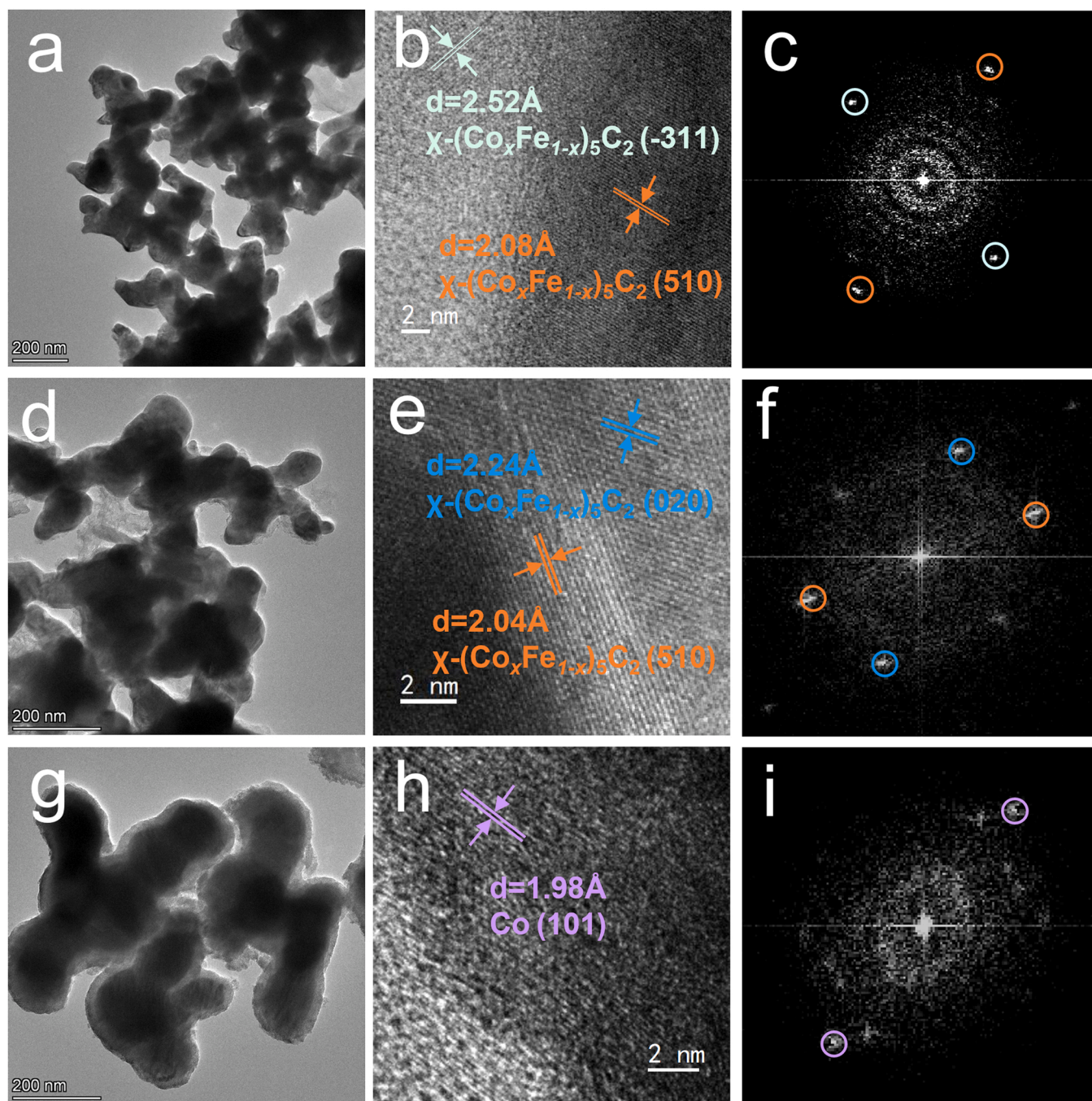


Fig. 6. TEM and HRTEM images of spent catalysts. (a, b, c) of Co1Fe2 catalyst; (d, e, f) of Co2Fe1 catalyst; (g, h, i) of Co1 catalyst.

by the difference in the phases of reduced catalysts (Fig. 4a), which can ultimately be attributed to the difference in proximity between Co and Fe in catalysts. The above discussion can be summarized as that the composition and proximity of Co and Fe in catalyst precursors are crucial for the reduction behavior of Co-Fe bimetallic catalysts.

### 3.4. Physicochemical properties of spent catalysts

The formation of various complex phases would be stimulated after the reduced phases were exposed to the reaction atmosphere of  $\text{CO}_2$  and  $\text{H}_2$ . Therefore, XRD, TEM and MES measurements were conducted to examine the structural and compositional changes of catalysts after  $\text{CO}_2$  hydrogenation experiments for 24 h. First, the crystal structures of spent catalysts with different Co/Fe molar ratios were determined by XRD, as

shown in Fig. 5a, b. According to the XRD patterns of spent Fe1 catalyst, the diffraction peaks can be obviously attributed to the  $\text{Fe}_5\text{C}_2$  (JCPDS 01-089-2544) and  $\text{Fe}_3\text{O}_4$  (JCPDS 01-088-0866) phases, which are two important active sites for catalyzing the synthesis of olefins from  $\text{CO}_2$  hydrogenation over Fe-based catalysts [46]. With the presence of Co element, the completely vanishing of  $\text{Fe}_3\text{O}_4$  diffraction peak at  $35.5^\circ$  are observed in the spent Co-Fe bimetallic catalysts. At the same time, the diffraction peaks at  $43.5$  and  $44.2^\circ$  originally attributed to the  $\text{Fe}_5\text{C}_2$  phase are observed to become weaker and shift toward higher  $2\theta$  angles with the increase of Co/Fe in catalyst. This is due to the smaller radius Co element being doped into the  $\text{Fe}_5\text{C}_2$  lattice to replace the position of the Fe element, resulting in the formation of  $\chi-(\text{Co}_x\text{Fe}_{1-x})_5\text{C}_2$  structure, which shrinks the lattice and shifts the position of the corresponding diffraction peaks toward  $2\theta$  increase [29,30,36]. Based on the above

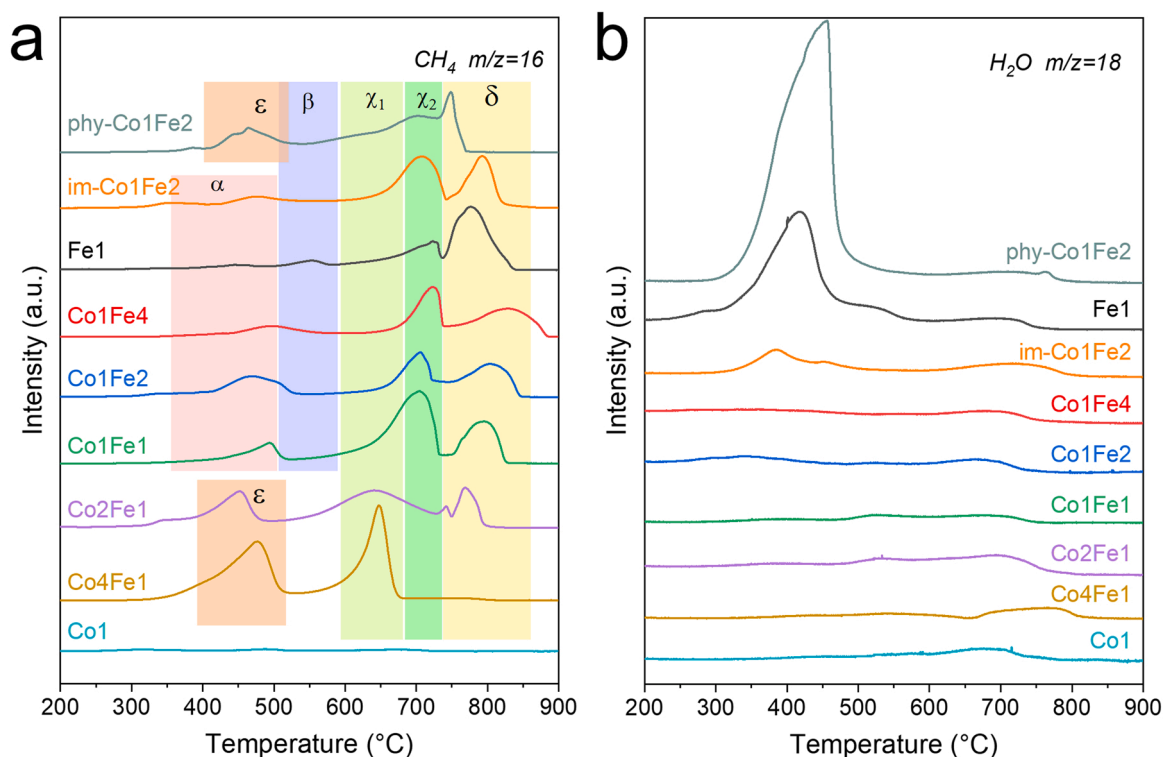


Fig. 7. Temperature-programmed hydrogenation (TPH) spectra of the spent catalysts. a)  $\text{CH}_4$  signal, b)  $\text{H}_2\text{O}$  signal.

discussion, we can draw a conclusion that the  $(\text{Co}_x\text{Fe}_{1-x})_5\text{C}_2$  alloy carbide species is the unique iron species in spent co-precipitated Co-Fe bimetallic catalysts. In addition, the existence of other metal carbides in the bulk phase is also detected. The  $\text{Co}_2\text{C}$  phase with characteristic peaks at  $45.8$  and  $41.3^\circ$  (JCPDS 01–072–1369) becomes dominant phase for spent  $\text{Co4Fe1}$  and  $\text{Co2Fe1}$  catalysts. Furthermore, the diffraction peaks of the spent  $\text{im-Co1Fe2}$  catalyst can be attributed to the  $\chi$ – $(\text{Co}_x\text{Fe}_{1-x})_5\text{C}_2$  alloy carbide phase, which is similar to that of  $\text{Co1Fe2}$  catalyst. However, the lower  $2\theta$  offset at about  $43.5$  and  $44.2^\circ$  of  $\text{im-Co1Fe2}$  catalyst reflects that the lower doping amount of Co element in  $\chi$ – $(\text{Co}_x\text{Fe}_{1-x})_5\text{C}_2$  structure than that of  $\text{Co1Fe2}$  catalyst. As for the spent  $\text{phy-Co1Fe2}$  catalyst, the diffraction peaks can be attributed to  $\text{Fe}_3\text{O}_4$ ,  $\chi$ – $(\text{Co}_x\text{Fe}_{1-x})_5\text{C}_2$  and  $\text{Co}_2\text{C}$  phases, which is different with that of the spent  $\text{Co1Fe2}$  catalyst, further indicating the proximity of Co and Fe in precursor is relevant to the structural evolution of catalysts during  $\text{CO}_2$  hydrogenation. For the spent  $\text{Co1}$  catalyst, three characteristic diffraction peaks at  $41.6$ ,  $44.5$  and  $47.5^\circ$  attributed to the  $\text{hcp-Co}$  phase (JCPDS 01–089–7373) are observed, which is identical to the structure of the reduced  $\text{Co1}$  catalyst, indicating the formation of  $\text{Co}_2\text{C}$  phase from metallic Co is inhibited under the reaction conditions. This phenomenon can be explained from previous reports that CO obtained from RWGS reactions can induce the formation of cobalt carbides [13], however, the low CO selectivity (4.0%) over the  $\text{Co1}$  catalyst is difficult to induce above transformation, resulting in the dominant  $\text{CH}_4$  (55.3%) in products.

The dynamic structural evolutions of  $\text{Co1Fe2}$  and  $\text{Fe1}$  catalysts during  $\text{CO}_2$  hydrogenation reaction were conducted on *in situ* XRD experiments, which is illustrated in Fig. S6. After comparison, no diffraction peak attributed to  $\text{Fe}_3\text{O}_4$  phase is found in  $\text{Co1Fe2}$  catalyst, while a subtle diffraction peak at  $35.5^\circ$  attributed to  $\text{Fe}_3\text{O}_4$  is detected in  $\text{Fe1}$  catalyst, which is consistent with the XRD results (Fig. 5a, b). For  $\text{Co1Fe2}$  catalyst (Fig. S6a), the diffraction peaks of the  $\text{Co}_x\text{Fe}_y$  alloy phase gradually weaken while the diffraction peaks of  $\chi$ – $(\text{Co}_x\text{Fe}_{1-x})_5\text{C}_2$  become obvious with the reaction time, and their intensity become about the same at 160 min. In comparison, the diffraction peaks of metallic Fe phase are still stronger than that of  $\text{Fe}_5\text{C}_2$  phase for  $\text{Fe1}$

catalyst until 240 min (Fig. S6b), indicating a lower carburizing ability for  $\text{Fe1}$  catalyst than  $\text{Co1Fe2}$  catalyst during the reaction process.

$^{57}\text{Fe}$  Mössbauer spectroscopy (MES) technique provides further insights into the proportion of iron species presented in spent catalysts and hence the composition of the active phase, shown in Fig. 5c, d and Table S6. For the spent  $\text{Fe1}$  catalyst, there are five sextets with hyperfine field (Hhf) of 184, 216 and 110 kOe attributed to typifying  $\chi$ – $\text{Fe}_5\text{C}_2$  (I, II and III) phase and the Hhf of 488 and 457 kOe attributed to  $\text{Fe}_3\text{O}_4$  (A and B) respectively as well as another doublet with  $\text{IS} = 0.24$  mm/s and  $\text{QS} = 1.11$  mm/s attributed to  $\text{Fe}^{3+}$ , exhibiting the coexistence of  $\chi$ – $\text{Fe}_5\text{C}_2$  (84.4%) and  $\text{Fe}_3\text{O}_4$  (13.7%) during  $\text{CO}_2$  hydrogenation [47,48]. For the spent  $\text{Co1Fe2}$  and  $\text{Co2Fe1}$  catalysts, no  $\text{Fe}_3\text{O}_4$  phase is detected, and the three sextets can be attributed to  $\chi$ – $\text{Fe}_5\text{C}_2$  within a reasonable range, which is in accord with the discussion about XRD pattern (Fig. 5a, b). The detailed Mössbauer parameters shown in Table S6 exhibit the main iron phases in  $\text{Fe1}$ ,  $\text{Co1Fe2}$ ,  $\text{Co2Fe1}$ ,  $\text{im-Co1Fe2}$  and  $\text{phyCo1Fe2}$  catalysts. It is worth paying more attention that the corresponding Hhf values of iron carbides decrease markedly with increasing Co content in Co-Fe bimetallic catalysts. For example, the Hhf value of  $\chi$ – $\text{Fe}_5\text{C}_2$  (III) goes from 110 kOe ( $\text{Fe1}$ ) to 104 kOe ( $\text{Co1Fe2}$ ) and further to 93 kOe ( $\text{Co2Fe1}$ ), implying that the C/Fe molar ratio in measured iron carbides increases, further justifying the formation of  $\chi$ – $(\text{Co}_x\text{Fe}_{1-x})_5\text{C}_2$  alloy carbide [36,49]. The proportion of  $\chi$ – $(\text{Co}_x\text{Fe}_{1-x})_5\text{C}_2$  alloy carbide in spent  $\text{Co1Fe2}$  catalyst is determined to be 97.2%, which is higher than those of spent  $\text{Co2Fe1}$  (84.4%) and spent  $\text{Fe1}$  catalyst (84.4%) (Fig. 5d). This suggests that the molar ratio of Co/Fe = 1/2 in the Co-Fe bimetallic catalyst is conducive to the formation of  $\chi$ – $(\text{Co}_x\text{Fe}_{1-x})_5\text{C}_2$ . For the spent  $\text{im-Co1Fe2}$  catalysts, three sextets with Hhf of 187 (I), 213 (II) and 107 kOe (III) can be attributed to  $\chi$ – $(\text{Co}_x\text{Fe}_{1-x})_5\text{C}_2$  phase, and the corresponding values are between those for  $\text{Fe1}$  and  $\text{Co1Fe2}$  catalysts. It suggests that the doping amount of Co element in  $\chi$ – $(\text{Co}_x\text{Fe}_{1-x})_5\text{C}_2$  alloy carbide in spent  $\text{im-Co1Fe2}$  catalyst is lower than that in spent  $\text{Co1Fe2}$  catalyst, which is consistent with the above discussion about  $2\theta$  offset. In addition, the iron species in spent  $\text{phy-Co1Fe2}$  catalyst mainly contain  $\chi$ – $(\text{Co}_x\text{Fe}_{1-x})_5\text{C}_2$  (54.9%) and  $\text{Fe}_3\text{O}_4$  40.1%) phases, which is markedly different with  $\text{Co1Fe2}$  catalyst. The above discussion further suggests

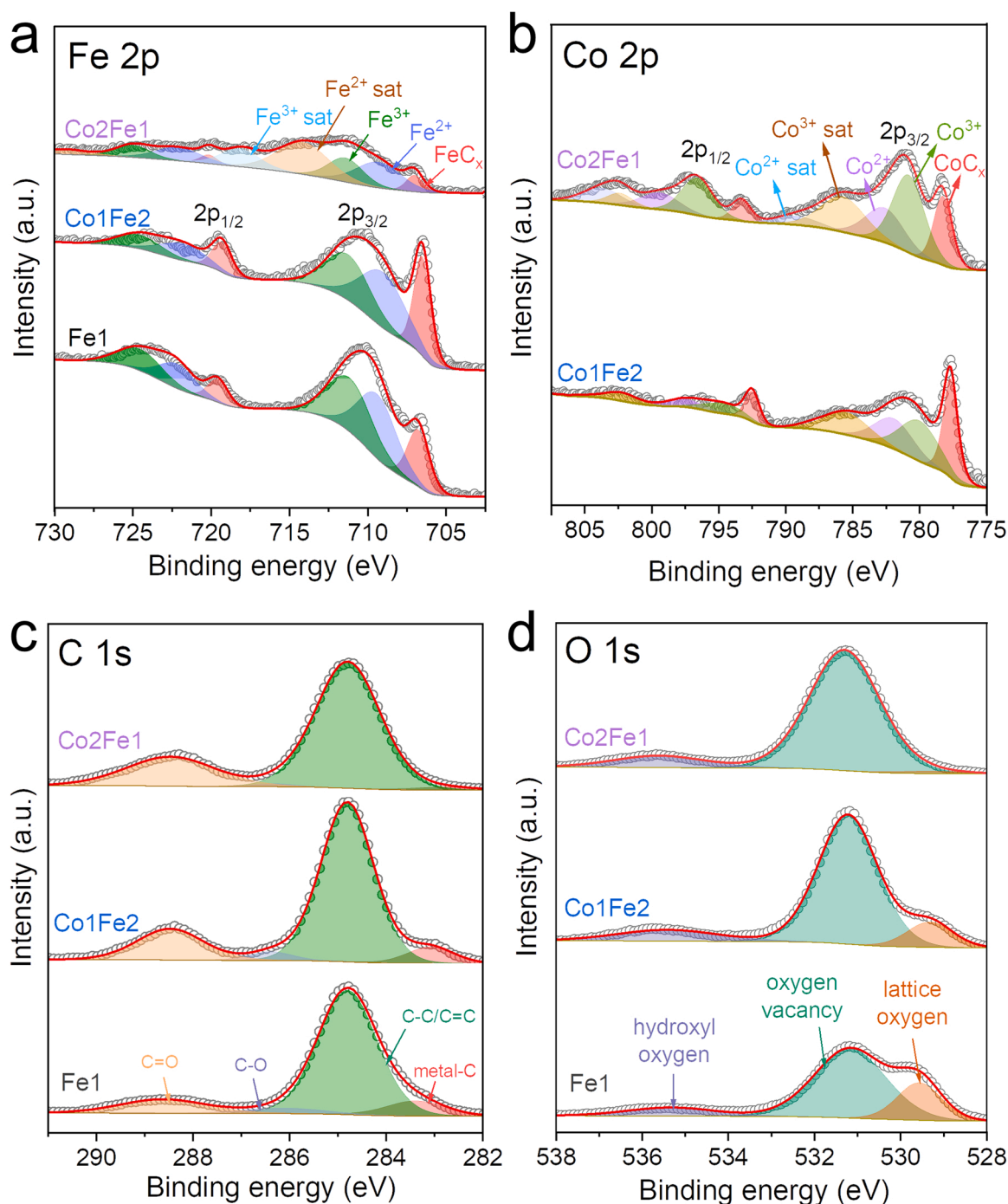


Fig. 8. XPS spectra of spent Fe1, Co1Fe2 and Co2Fe1 catalysts. a) Fe 2p, b) Co 2p, c) C 1 s, d) O 1 s.

that the  $\chi$ -(Co<sub>x</sub>Fe<sub>1-x</sub>)<sub>5</sub>C<sub>2</sub> is active phase for olefin synthesis, and the appropriate composition and proximity of Co-Fe bimetallic catalysts influence the structural evolution of  $\chi$ -(Co<sub>x</sub>Fe<sub>1-x</sub>)<sub>5</sub>C<sub>2</sub> phase.

TEM and HRTEM images of spent Co1Fe2, Co2Fe1 and Co1 catalysts are shown in Fig. 6. The HRTEM images of spent Co1Fe2 (Fig. 6b, c) and Co2Fe1 (Fig. 6e, f) catalysts confirm the existence of  $\chi$ -(Co<sub>x</sub>Fe<sub>1-x</sub>)<sub>5</sub>C<sub>2</sub>, based on their respective two sets of lattice fringes. This result can be an evidence to prove above points about the formation of iron carbide [30]. It also shows the presence of metallic Co as the active phase for Co1 catalyst (Fig. 6h, i), which is consistent with above XRD analysis (Fig. 5a, b). Furthermore, the EDS mappings images of spent Co1Fe2 catalyst present that all elements (Co, Fe, Na, O and C) are uniformly dispersed, as shown in Fig. S7. The textural properties of the spent catalysts with

different Co/Fe ratios were tested by N<sub>2</sub> adsorption-desorption experiments as shown in Fig. S8 and Table S7. According to Fig. S8a, after CO<sub>2</sub> hydrogenation reaction, all catalysts studied retain their type-H2 hysteresis loops typical of type IV isotherm. Compared with the textural properties of the corresponding calcined catalysts, the  $S_{\text{BET}}$  and  $V_{\text{total}}$  values of the spent catalysts decrease significantly (Table S7), and the pore size distributions are mainly concentrated in smaller sizes of less than 10 nm (Fig. S8b). The noticeable changes can be ascribed to catalyst aggregation or carbon disposition in combination with TEM of calcined (Fig. 3a, d, g), and spent (Fig. 6a, d, g) catalysts [50]. However, as the molar ratio of Co/Fe increases in the spent catalysts, the  $S_{\text{BET}}$  and  $V_{\text{total}}$  present a similar volcanic-type trend as the calcined catalysts with the maximum value of spent Co1Fe1 catalyst. In general, the formation



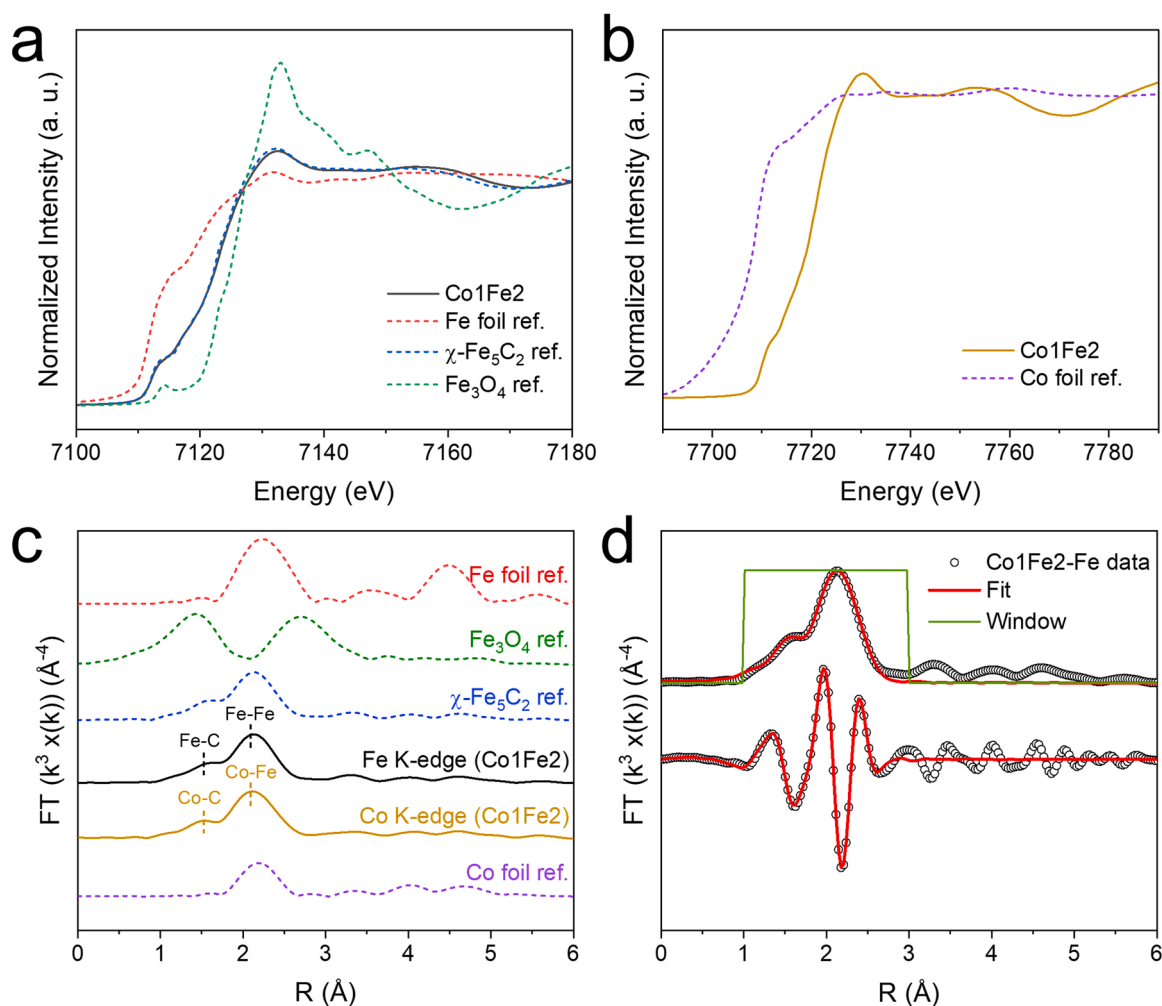


**Fig. 9.** Coordination environment analysis of the spent Co1Fe2 catalyst. Normalized XANES spectra of the spent Co1Fe2 catalyst at Fe K-edge (a) and Co K-edge (b). c)  $k^3$ -weighted Fourier transformed EXAFS spectra of the spent Co1Fe2 catalyst. d) The FT EXAFS and the fitted spectrum at Fe K-edge of the spent Co1Fe2 catalyst.

of Co-Fe bimetallic catalysts is conducive to increasing the exposure of active sites.

Temperature-programmed hydrogenation (TPH) in conjunction with mass spectroscopy was also performed to probe the formation of oxide and carbon species in spent catalysts. Fig. 7 presents TPH spectra for spent catalysts with  $m/z = 16$  (a) and  $m/z = 18$  (b), corresponding to the response signals of  $\text{CH}_4$  and  $\text{H}_2\text{O}$ , respectively. Table S8 briefly describes the specific carbonation species and their peak temperature during hydrogenation corresponding to Fig. 7a, according to the previous reports [51,52]. For Fe1 catalyst, the largest peak of the  $\text{CH}_4$  signal locates at high temperature of  $780^\circ\text{C}$  (peak  $\delta$ ), which corresponds to the hydrogenation of carbon deposition [33]. The peak intensity decreases significantly with increasing Co content in Co-Fe bimetallic catalysts and almost disappears in Co4Fe1 catalyst, indicating that the addition of Co can improve the anti-carbon deposition ability of Fe-based catalysts. There is also a subpeak at relatively high temperature of  $720^\circ\text{C}$  (peak  $\chi_2$ ) attributed to crystalline carbide and a small shoulder peak at  $670^\circ\text{C}$  (peak  $\chi_1$ ) attributed to amorphous carbide observed in Fe1 catalyst, and these carbides all belong to  $\chi\text{-Fe}_5\text{C}_2$  [53]. With the increase of Co content in Co-Fe bimetallic catalysts, the total peak of cobalt-iron alloy carbide ( $\chi\text{-(Co}_x\text{Fe}_{1-x})_5\text{C}_2$ ) at  $595\text{--}795^\circ\text{C}$  (peak  $\chi_1$  and  $\chi_2$ ) moves to lower temperature. Specifically, the content of crystalline  $\chi\text{-(Co}_x\text{Fe}_{1-x})_5\text{C}_2$  alloy carbide (peak  $\chi_2$ ) first increases and then decreases, being highest in Co1Fe1 catalyst and approaching zero in Co4Fe1 catalyst, while the content of amorphous  $\chi\text{-(Co}_x\text{Fe}_{1-x})_5\text{C}_2$  alloy carbide (peak  $\chi_1$ ) gradually increases and eventually occupies the main  $\chi\text{-(Co}_x\text{Fe}_{1-x})_5\text{C}_2$  in spent

Co2Fe1 and Co4Fe1 catalysts. Based on the evaluation results of the catalysts for  $\text{CO}_2$  hydrogenation, we speculate that the crystalline  $\chi\text{-(Co}_x\text{Fe}_{1-x})_5\text{C}_2$  is the main active phase to produce olefins, which could explain why Co2Fe1 catalyst have similar proportion of  $\chi\text{-(Co}_x\text{Fe}_{1-x})_5\text{C}_2$  alloy carbide to Fe1 catalysts (Fig. 5d) but presents different catalytic performance. Furthermore, a main peak appearing at about  $480^\circ\text{C}$  (peak  $\epsilon$ ) attributed to the hydrogenation of  $\text{Co}_2\text{C}$  can be observed in Co2Fe1 and Co4Fe1 catalysts, which is consistent with the XRD results (Fig. 5a, b), and this intensive peak for Co4Fe1 catalyst locates at  $480^\circ\text{C}$ ,  $30^\circ\text{C}$  higher than that for Co2Fe1 catalyst, manifesting the increased crystallinity of  $\text{Co}_2\text{C}$  for Co4Fe1 catalyst. For the im-Co1Fe2 catalyst, the hydrogenation spectra are similar to that of spent Co1Fe4, Co1Fe2 and Co1Fe1 catalysts, which can be due to the fact that they all possess the unique  $\chi\text{-(Co}_x\text{Fe}_{1-x})_5\text{C}_2$  alloy carbide phase. Furthermore, the TPH spectra of  $\text{CH}_4$  and  $\text{H}_2\text{O}$  signal for spent phy-Co1Fe2 catalyst present a clear difference with that of Co1Fe2 catalyst, which could be ascribed to the different proximity between Co and Fe in catalysts. In addition, the main peak of  $\text{H}_2\text{O}$  signal at  $415^\circ\text{C}$  attributed to the hydrogenation of  $\text{Fe}_3\text{O}_4$  can be observed in Fe1 and phy-Co1Fe2 catalysts, suggesting the existence of  $\text{Fe}_3\text{O}_4$  phase. Moreover, as expected, there are no obvious carbide and oxide response curves on the spent Co1 catalyst during the TPH experiment, indicating the presence of metallic Co alone. These discussions above are consistent with the results of MES and XRD of spent catalysts (Fig. 5).

The chemical state and surface structure analysis were studied on spent catalysts using XPS measurements, shown in Fig. 8. The Fe 2p



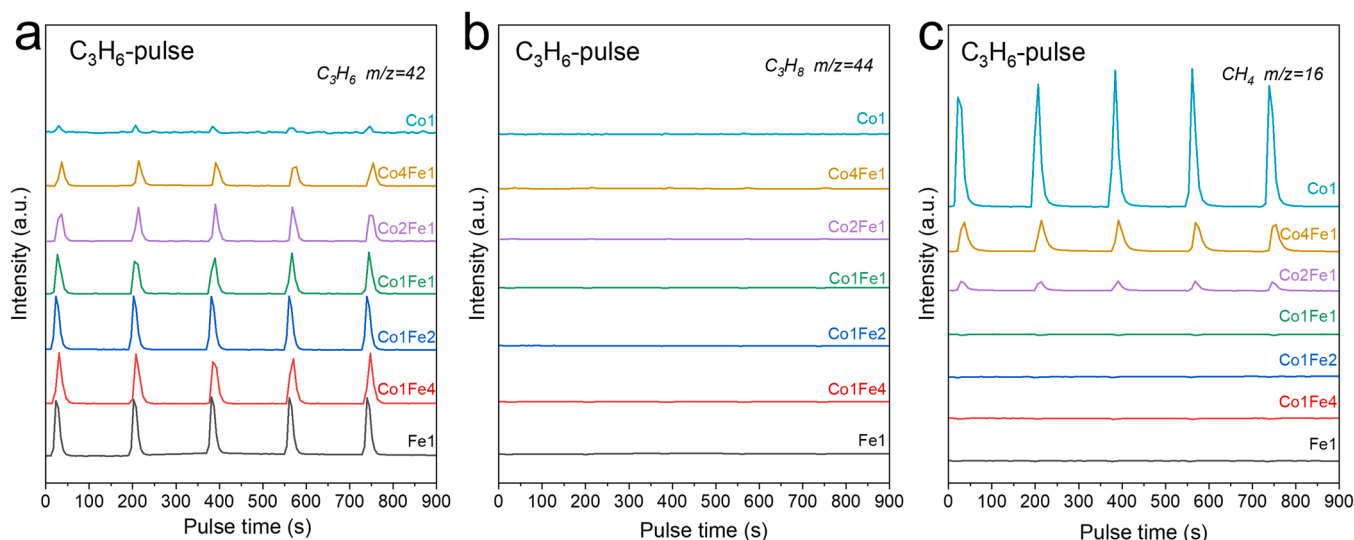


Fig. 10.  $C_3H_6$ -pulse transient hydrogenation spectra of the spent catalysts. a)  $C_3H_6$  signal, b)  $C_3H_8$  signal, c)  $CH_4$  signal.

spectra of spent Fe1, Co1Fe2 and Co2Fe1 catalysts exhibit two peaks at 706.6 eV ( $2p_{3/2}$ ) and 719.6 eV ( $2p_{1/2}$ ) as shown in Fig. 8a, which are associated with iron carbide species (denoted as  $FeC_x$ ) [20,54]. According to the discussion of XRD and MES on spent catalysts, the  $FeC_x$  species on spent monometallic Fe1 and bimetallic Co-Fe catalysts are derived from  $\chi-(Co_xFe_{1-x})_5C_2$ . A pair of minor peaks at 777.8 eV ( $2p_{3/2}$ ) and 792.5 eV ( $2p_{1/2}$ ) presented in spent bimetallic Co-Fe catalysts can be attributed to cobalt carbide species (denoted as  $CoC_x$ ) [36,55], which could originate from  $\chi-(Co_xFe_{1-x})_5C_2$  alloy carbide or  $CoC_2$  species formed during  $CO_2$  hydrogenation, shown in Fig. 8b. As seen in Fig. S9-13 and Table S9, which is summarized by deconvolution of XPS spectra, the content of  $FeC_x$  and  $CoC_x$  in Co1Fe2 catalyst is higher than those in other catalysts studied in different depths. Take the surface composition analysis of catalyst as an example, the  $FeC_x$  proportion (in all Fe species) in spent Co1Fe2 catalyst is determined to be 27.3%, higher than that in spent Fe1 (15.9%) and Co2Fe1 (6.7%) catalysts, and the  $CoC_x$  proportion (in all Co species) in spent Co1Fe2 catalyst (28.1%) is higher than that in Co2Fe1 catalyst (18.2%). This indicates that Co1Fe2 catalyst is beneficial to the formation of both  $FeC_x$  and  $CoC_x$  species, which can be further attributed to  $\chi-(Co_xFe_{1-x})_5C_2$ . Furthermore, the  $CoC_x$  proportion (28.1% in all Co species) in spent Co1Fe2 catalyst is close to the  $FeC_x$  proportion (27.3% in all Fe species), while the  $CoC_x$  proportion in spent Co2Fe1 (18.2%) and phy-Co1Fe2 (33.7%) catalyst respectively are much higher than their  $FeC_x$  proportion (6.7%, 7.7%), respectively, which can give evidence for the formation of  $Co_2C$  except  $\chi-(Co_xFe_{1-x})_5C_2$  phase in spent Co2Fe1 and phy-Co1Fe2 catalysts. Furthermore, it's worth noting that the content of  $CoC_x$  in im-Co1Fe2 catalyst is lower than that in Co1Fe2 catalysts in different depths, indicating the doping amount of Co element into  $\chi-(Co_xFe_{1-x})_5C_2$  alloy carbide in spent im-Co1Fe2 catalyst is lower than that in spent Co1Fe2 catalysts, which is consistent with the results of XRD and MES over spent catalysts (Fig. 5). The discussion above can be summed up as that Co-Fe bimetallic catalyst with a molar ratio of Co/Fe = 1/2 has a pronounced effect on the formation of  $\chi-(Co_xFe_{1-x})_5C_2$  alloy carbide during  $CO_2$  hydrogenation reaction.

High-resolution spectra of C 1s (Fig. 8c) exhibit four characteristic peaks at 283.1, 284.8, 286.4 and 288.5 eV, which are attributed to metal-C, C-C/C=C, C-O and C=O species, respectively. As shown in Table S9, the relative content of metal-C species in Co1Fe2 catalyst surpasses other catalysts we studied in different depths. For example, the relative content of metal-C species on the surface of spent Co1Fe2 catalyst is determined to be 8.1%, higher than that of Fe1 (6.6%), Co2Fe1 (1.5%), im-Co1Fe2 (6.2%), phy-Co1Fe2 (4.0%) catalysts, which

confirms a good carburization ability for Co1Fe2 catalyst. In addition, metal-C species all present an increasing relative content with depth in spent catalysts investigated, as shown in Fig. S14a and Table S9, indicating that carburization is more concentrated on the bulk of catalyst. The high-resolution spectra of O1s can be ascribed to three characteristic peaks of hydroxyl oxygen (535.4 eV), oxygen vacancy (531.2 eV) and lattice oxygen (529.3 eV), respectively (Fig. 8d). In different depths (Fig. S14b and Table S9), the relative contents of oxygen vacancy (in all oxygen species) present an arresting trend of Fe1 < Co1Fe2 < Co2Fe1, indicating that the addition of Co element can promote the formation of surface oxygen vacancy, further proving that cobalt-iron bimetallic catalyst is effective to enhance  $CO_2$  adsorption and improve catalytic activity [56].

X-ray absorption spectroscopy (XAS) at Fe K-edge and Co K-edge were conducted on the spent Co1Fe2 catalyst to characterize the coordination environment of Fe and Co atoms. In Fig. 9a, the X-ray absorption near-edge structure (XANES) spectrum of the Co1Fe2 sample at Fe K-edge coincides with the reference  $\chi-Fe_5C_2$ . The XANES spectrum of the Co1Fe2 sample at Co K-edge (Fig. 9b) indicates the existence of high valence for Co atom [39]. The Fourier transformed extended X-ray absorption fine structure (EXAFS) spectra of the spent Co1Fe2 catalyst at Fe K-edge is almost the same with the line shape of the reference  $\chi-Fe_5C_2$  (Fig. 9c), demonstrating that  $Fe_5C_2$  species are formed during reaction. Meantime, the spectrum at Fe K-edge is very similar to that at Co K-edge indicating that part of Fe atoms is substituted by Co atoms. Furthermore, both the spectra at the Fe K-edge (Fig. 9d) and Co K-edge (Fig. S15) for the spent Co1Fe2 catalyst can be well fitted using  $Fe_5C_2$  structure as the model (Table S10). The structure of the first shell (Co-C) and the second shell (Co-Fe) are similar to those in  $\chi-Fe_5C_2$  (Fe-C and Fe-Fe, respectively), which hints to the formation of  $\chi-(Co_xFe_{1-x})_5C_2$  alloy carbide. The XAS results prove that Co doping into the structure of  $\chi-Fe_5C_2$  to form  $\chi-(Co_xFe_{1-x})_5C_2$  alloy carbide in Co-Fe bimetallic catalyst, which are consistent to the XRD, MES and XPS results.

### 3.5. Adsorption and surface reactivity behavior

Pulse transient hydrogenation experiments were performed on the spent catalysts with different Co/Fe ratios to examine the secondary hydrogenation ability by using  $C_3H_6$  as study gas. Fig. 10 presents pulse transient hydrogenation spectra for spent catalysts with response signal of  $C_3H_6$ ,  $C_3H_8$  and  $CH_4$ . It exhibits similar high intensity of  $C_3H_6$  signal peaks for Fe1, Co1Fe4, Co1Fe2 and Co1Fe1 catalysts and weakened  $C_3H_6$  signal peaks with increasing the molar ratio of Co/Fe for Co2Fe1,

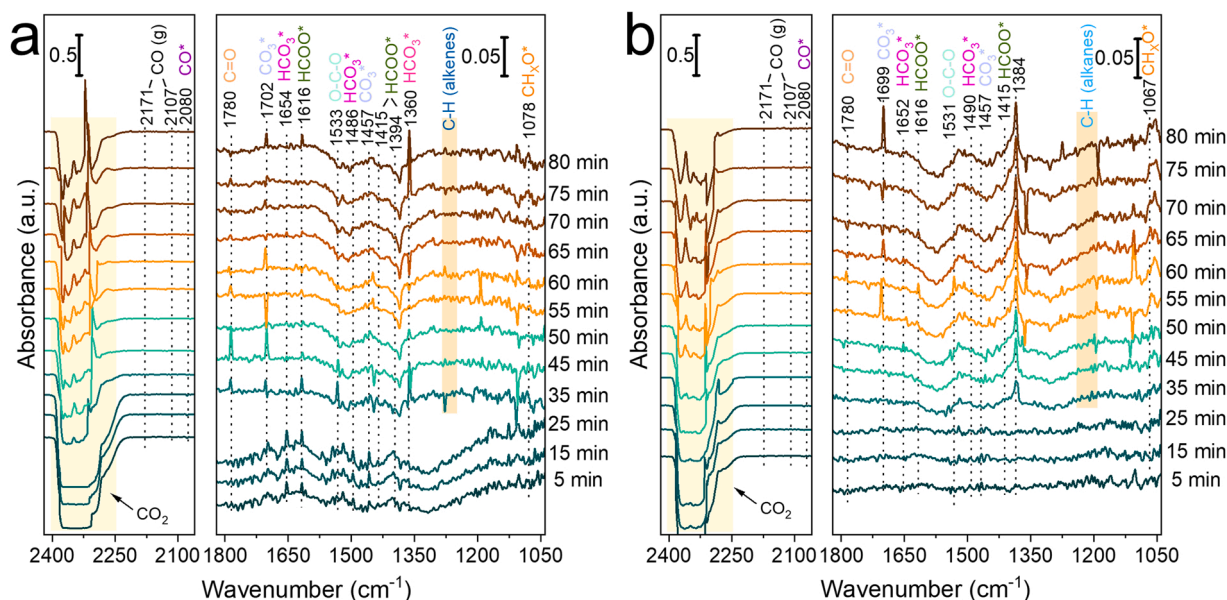


Fig. 11. *In situ* high pressure DRIFTS spectra of a) Co1Fe2 and b) Co1 catalyst.

Co4Fe1 and Co1 catalysts. All spent catalysts studied reveal the weak capacity of secondary hydrogenation to  $C_3H_8$  reflected by those low  $C_3H_8$  response signal, indicating that the re-adsorbed  $C_3H_6$  can react to form other products via secondary hydrogenation. It is worth noting that there is no obvious  $CH_4$  signal peak detected on Fe1, Co1Fe4, Co1Fe2 and Co1Fe1 catalysts, whereas the  $CH_4$  signal peaks on Co2Fe1, Co4Fe1 and Co1 catalysts appear an increasing trend with increasing Co content, demonstrating that Co2Fe1, Co4Fe1 and Co1 catalysts have the ability of hydrocracking the re-adsorbed  $C_3H_6$  to  $CH_4$ . In summary, the re-absorption of  $C_3H_6$  on Fe1, Co1Fe4, Co1Fe2 and Co1Fe1 catalysts does not occur, while the re-absorption of  $C_3H_6$  on Co4Fe1, Co2Fe1 and Co1 catalysts has the potential to be hydrocracked to  $CH_4$ . These results explain why the olefin selectivity on Fe1, Co1Fe4, Co1Fe2 and Co1Fe1 catalysts is relatively high, while the olefin selectivity decreases sharply on the catalysts with higher Co content, along with the higher  $CH_4$  and lower  $C_{5+}$ .

$CO_2$ -TPD experiments were performed to examine the adsorption behavior of the reduced catalysts. Both  $CO_2$  and CO signals are detected for comparison as shown in Fig. S16, due to the fact that the adsorbed  $CO_2$  can react with the pre-reduced catalysts to release CO. The weak  $CO_2$  desorption peaks and almost no CO release peaks below 300 °C are detected on all catalysts, indicating that there is less  $CO_2$  in the form of physical adsorption on the catalysts [57]. The main peaks above 500 °C attributed to strongly adsorbed  $CO_2$  are observed on reduced catalysts, especially in Co2Fe1, Co4Fe1 and Co1 catalysts, which provides favorable evidence for their higher  $CO_2$  conversion. In order to explore the essential reason for the higher STY of olefins over Co1Fe2 catalyst, the  $CO$ -TPD experiments were performed on the reduced Fe1 and Co1Fe2 catalysts. As shown in Fig. S17 and Table S11, the total adsorbed CO on Co1Fe2 catalyst is 1.55 times higher than that on Fe1 catalyst, and the CO desorption behavior of the strongly adsorbed CO on Co1Fe2 catalyst is detected at relatively lower temperature than that on Fe1 catalyst, indicating that Co1Fe2 catalyst presents stronger CO desorption ability than Fe1 catalyst. It further proves that the active CO intermediate adsorbed on the  $\chi-(Co_xFe_{1-x})_5C_2$  active site over Co1Fe2 catalyst is easily converted to hydrocarbons, which further provides sufficient evidence for its higher  $CO_2$  conversion and lower CO selectivity.

To explore the adsorbed reaction intermediates and reactivity during  $CO_2$  hydrogenation, *in situ* high pressure DRIFTS measurements were conducted on the calcined Co1Fe2 and Co1 catalysts. After injecting the reaction gas, obvious signals assigned to the surface carbonate species

( $CO_3^*$ , ca. 1457, 1702  $cm^{-1}$ ), the carbonate species ( $HCO_3^*$ , ca. 1360, 1486, 1654  $cm^{-1}$ ) and the formate species ( $HCOO^*$ , ca. 1394, 1415, 1616  $cm^{-1}$ ) are immediately detected on Co1Fe2, which are generated from the interaction between the adsorbed  $CO_2$  and surface oxygen vacancies [54,58,59]. As reaction proceeds in Co1Fe2 catalyst, the  $HCO_3^*$  bond at 1486 and 1654  $cm^{-1}$  become indistinct at 35 min, accompanied by the appearance of the O-C-O stretching of  $HCOO^*$  at 1533  $cm^{-1}$  and the C=O of  $HCOO^*$  at 1780  $cm^{-1}$  [10,60]. A band at 2070  $cm^{-1}$  associated with the chemisorbed  $CO^*$  is detectable in Co1Fe2 catalyst, which is generated from the  $HCOO^*$  species [61]. Meanwhile, the C-H (1298–1342  $cm^{-1}$ ) stretching of alkenes gradually becomes strengthen, which is essential intermediates for  $CO_2$  hydrogenation to olefins. However, in Co1 catalyst, the signal of  $HCO_3^*$ ,  $CO_3^*$  and  $HCOO^*$  species is imperceptible until the reaction gas has been injected for 30 min. With the reaction proceeding in Co1 catalyst, the signal intensity of  $HCOO^*$  species (1384, 1415  $cm^{-1}$ ) gradually becomes stronger and finally stronger than that in Co1Fe2 catalyst, which can explain the higher  $CO_2$  conversion on Co1 catalyst [10]. Besides, the C-H stretching of alkanes (1233–1287  $cm^{-1}$ ) is detected in Co1 catalyst. An obvious signal of  $CH_xO^*$  species (1067  $cm^{-1}$ ) is observed in Co1 catalyst, which is considered as the crucial intermediate species for  $CO_2$  methanation, while the intensity of this species is diminished in Co1Fe2 catalyst, suggesting that the Co1Fe2 catalyst presents a lower activity toward  $CO_2$  methanation [24]. The results of *in situ* DRIFT could further verify the high olefin selectivity in Co1Fe2 catalyst and the high  $CH_4$  selectivity in Co1 catalyst. Therefore, based on above discussion, a possible reaction pathway for  $CO_2$  hydrogenation to olefins over Co-Fe bimetallic catalysts is proposed as follow. First,  $CO_2$  is adsorbed and activated on the  $\chi-(Co_xFe_{1-x})_5C_2$  active site and then converted into the  $CO^*$  species, going through multiple intermediates ( $CO_3^*$ ,  $HCO_3^*$ ,  $HCOO^*$ ). Then, the  $CO^*$  species is dissociated and hydrogenated to form  $CH_x$  species, where the  $CH_x$  species can be coupled with other  $CH_x$  adsorbents to further form olefins ( $C_nH_{2n}$ ), which is a possible reaction pathway over Co1Fe4, Co1Fe2 and Co1Fe1 catalysts with  $\chi-(Co_xFe_{1-x})_5C_2$  as the active phase. However, over Co-Fe bimetallic catalysts with the molar ratio of Co/Fe exceeding 1/1, the  $CH_x$  species tends to be further hydrogenated to  $CH_4$  or the adsorbed olefin may be further hydrogenated to paraffins ( $C_nH_{2n+2}$ ). (Fig. 11).

Based on above discussion, the structural evolution process of Co-Fe bimetallic catalysts is demonstrated by Fig. 12. The catalysts (Co1Fe4, Co1Fe2, Co1Fe1, Co2Fe1 and Co4Fe1) prepared by precipitation

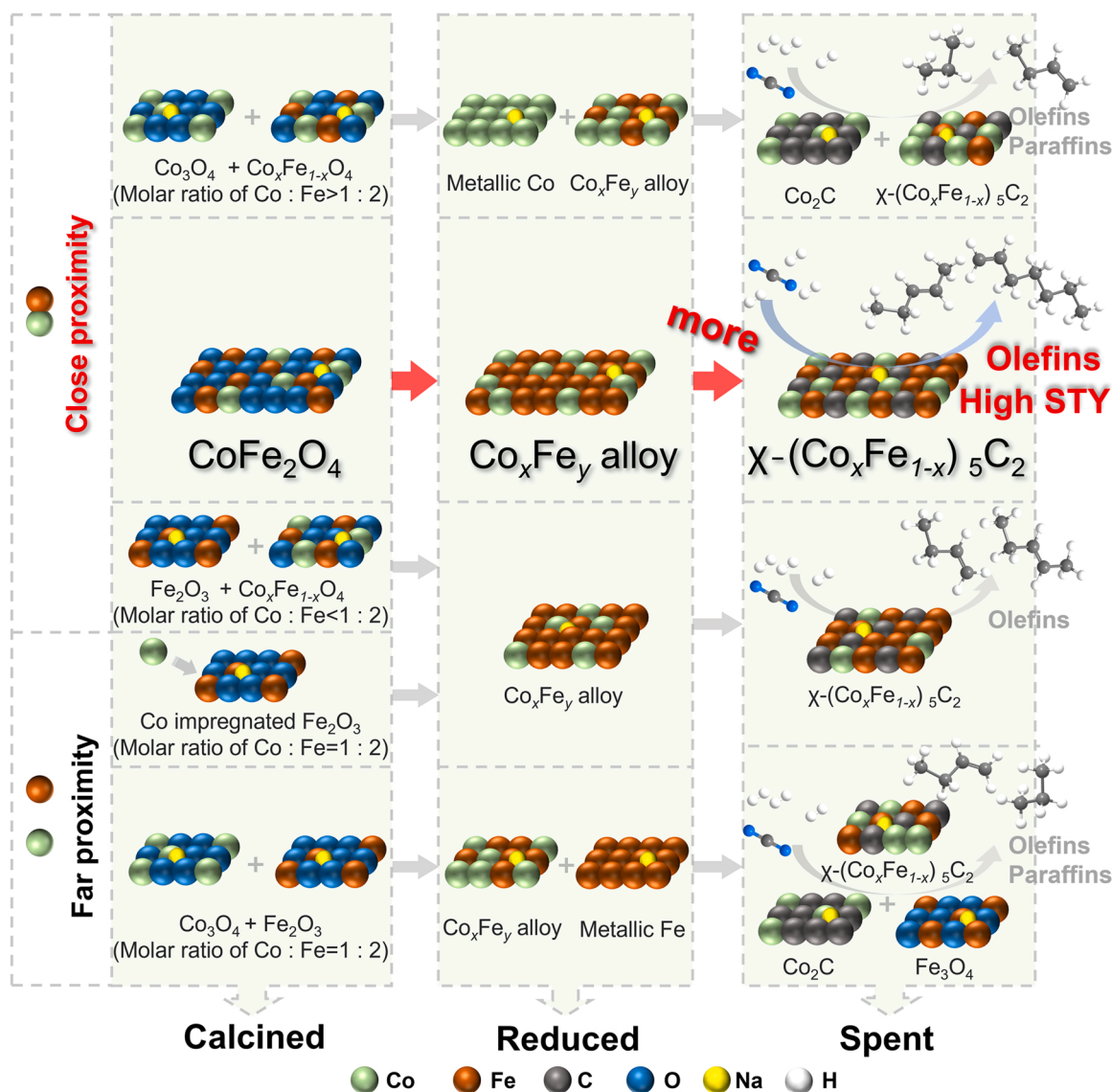


Fig. 12. Schematic diagram of structural evolution over Co-Fe bimetallic catalysts.

method have the close proximity between Co and Fe elements. The Co1Fe2 catalyst with a Co/Fe molar ratio of 1/2 possesses a sole CoFe<sub>2</sub>O<sub>4</sub> phase in precursor, which could be converted to Co<sub>x</sub>Fe<sub>y</sub> alloy phase during reduction process and finally to  $\chi$ -(Co<sub>x</sub>Fe<sub>1-x</sub>)<sub>5</sub>C<sub>2</sub> alloy carbide phase as the active site for higher performance of olefin synthesis during reaction process. However, the CoFe<sub>2</sub>O<sub>4</sub> spinel structure is not the only phase detected for other calcined Co-Fe bimetallic catalysts with molar ratio of Co/Fe deviating from 1/2, but also accompanied by  $\alpha$ -Fe<sub>2</sub>O<sub>3</sub> phase for the catalysts with Co/Fe less than 1/2 or Co<sub>3</sub>O<sub>4</sub> phase for the catalysts with Co/Fe more than 1/2. For the catalysts with Co/Fe less than 1/2, the calcined Co<sub>x</sub>Fe<sub>3-x</sub>O<sub>4</sub> and Fe<sub>2</sub>O<sub>3</sub> could be converted to Co<sub>x</sub>Fe<sub>y</sub> alloy phase during reduction process and finally to  $\chi$ -(Co<sub>x</sub>Fe<sub>1-x</sub>)<sub>5</sub>C<sub>2</sub> alloy carbide during reaction process. For the catalysts with Co/Fe more than 1/2, the calcined catalysts present the coexistence of Co<sub>x</sub>Fe<sub>3-x</sub>O<sub>4</sub> and Co<sub>3</sub>O<sub>4</sub> phases, which could be converted to fcc-Co and Co<sub>x</sub>Fe<sub>y</sub> alloy phase after reduction and finally to Co<sub>2</sub>C and  $\chi$ -(Co<sub>x</sub>Fe<sub>1-x</sub>)<sub>5</sub>C<sub>2</sub> alloy carbide after reaction. The im-Co1Fe2 catalyst with a Co/Fe molar ratio of 1/2 is prepared by impregnating Fe<sub>2</sub>O<sub>3</sub> with Co<sup>3+</sup> solution, where the interaction between Co and Fe in precursor is relatively weaker than that of Co1Fe2 catalyst. The im-Co1Fe2 catalyst could be converted to Co<sub>x</sub>Fe<sub>y</sub> alloy phase during reduction process and finally to  $\chi$ -(Co<sub>x</sub>Fe<sub>1-x</sub>)<sub>5</sub>C<sub>2</sub> alloy carbide during reaction process, while

the doping amount of Co element into  $\chi$ -(Co<sub>x</sub>Fe<sub>1-x</sub>)<sub>5</sub>C<sub>2</sub> alloy carbide is lower than that in spent Co1Fe2 catalyst, which is not conducive to enhancing catalytic activity. In addition, the phy-Co1Fe2 with far proximity of Co and Fe in precursor is first converted to the coexistence of Fe metal and Co<sub>x</sub>Fe<sub>y</sub> alloy phases after reduction, and further to the coexistence of  $\chi$ -(Co<sub>x</sub>Fe<sub>1-x</sub>)<sub>5</sub>C<sub>2</sub>, Fe<sub>3</sub>O<sub>4</sub> and Co<sub>2</sub>C phases during the reaction.

#### 4. Conclusion

In summary, the crucial role of the composition and proximity of Co and Fe in Co-Fe bimetallic catalysts for structural evolution in CO<sub>2</sub> hydrogenation has been systematically investigated in this report. In catalytic performance, the Co1Fe2 catalyst prepared by coprecipitation and a following hydrothermal treatment presents a superior performance for olefin synthesis than other catalysts with same preparation method but different Co/Fe molar ratios and catalysts with different proximity but a same Co/Fe molar ratio of 1/2. At the same time, the STY of Co1Fe2 catalyst increases stunningly to 1810.8 mg·g<sub>cat</sub><sup>-1</sup>·h<sup>-1</sup> at the GHSV of 80000 mL·g<sub>cat</sub><sup>-1</sup>·h<sup>-1</sup>, which is higher than that over Fe-based catalyst. The *in/ex-situ* XRD, MES, TPH, XPS and H<sub>2</sub>-TPR analysis results provide relatively consistent evidence for the structural evolution of the catalysts



during the reduction and reaction processes. To be specific, the H<sub>2</sub>-TPR and *in/ex-situ* XRD experiments prove that the addition of Co elements could improve the reducibility of catalysts. The *in/ex-situ* XRD, MES, TPH and XPS analysis results show that Co1Fe2 catalyst with a sole spinel structure of CoFe<sub>2</sub>O<sub>4</sub> in precursor exhibits a much more remarkable content of (Co<sub>x</sub>Fe<sub>1-x</sub>)<sub>5</sub>C<sub>2</sub> alloy carbide (97.2%). The structural evolution path of Co1Fe2 catalyst can be summarized as follows: CoFe<sub>2</sub>O<sub>4</sub> → (Co<sub>x</sub>Fe<sub>y</sub>)O → Co<sub>x</sub>Fe<sub>y</sub> →  $\chi$ -(Co<sub>x</sub>Fe<sub>1-x</sub>)<sub>5</sub>C<sub>2</sub>. However, the precursors with the Co/Fe molar ratio exceeding 1/2 are not conducive to the formation of  $\chi$ -(Co<sub>x</sub>Fe<sub>1-x</sub>)<sub>5</sub>C<sub>2</sub> alloy carbide but are more inclined to form the Co<sub>2</sub>C structure, resulting in poor performance on olefin synthesis. The proximity of Co and Fe element in Co-Fe bimetallic catalysts is also a non-negligible factor affecting the structural evolution during reduction and reaction process. The im-Co1Fe2 catalyst prepared by impregnating Fe<sub>2</sub>O<sub>3</sub> with Co<sup>3+</sup> solution and phy-Co1Fe2 catalyst prepared by simply physical mixing of Fe<sub>2</sub>O<sub>3</sub> and Co<sub>3</sub>O<sub>4</sub>, which have the same composition as Co1Fe2 catalyst, present a relatively weak interaction between Co and Fe in precursors. As a result, the alloying extent of Co<sub>x</sub>Fe<sub>y</sub> and  $\chi$ -(Co<sub>x</sub>Fe<sub>1-x</sub>)<sub>5</sub>C<sub>2</sub> carbide phase produced in the reduction and reaction process is different from that of Co1Fe2 catalyst, respectively, resulting in the inferior performance for olefin synthesis. Overall, the understanding of the relationship between catalytic performance and structural evolution of Co-Fe bimetallic catalysts is anticipated to provide references for the design of catalysts from CO<sub>2</sub> hydrogenation to olefins.

#### CRediT authorship contribution statement

**Na Liu:** Designed the experiment, Methodology, Investigation, Formal analysis, Writing – original draft. **Jian Wei:** Conceptualization, Methodology, Funding acquisition, Supervision, Writing – review & editing. **Jing Xu:** Visualization, Investigation. **Yang Yu:** Investigation. **Jiafeng Yu:** Formal analysis. **Yu Han:** Investigation. **Kai Wang:** Investigation. **Joshua Iseoluwa Orege:** Formal analysis. **Qingjie Ge:** Conceptualization, Methodology, Funding acquisition, Supervision, Writing – review & editing. **Jian Sun:** Supervision, Funding acquisition.

#### Declaration of Competing Interest

The authors declare that they have no known competing financial interests or personal relationships that could have appeared to influence the work reported in this paper.

#### Data availability

No data was used for the research described in the article.

#### Acknowledgements

This work was supported by the National Key Research and Development Program of China (2022YFA1504704), the Youth Innovation Promotion Association of Chinese Academy of Sciences (2020189), the Natural Science Foundation of Liaoning Province (2022-MS-027), the Youth Science and Technology Star Project Support Program of Dalian City (2021RQ123), and DICP (Grant: DICP I202138). We also thank the assistance of Dr. Rile Ge from the Center for Advanced Mössbauer Spectroscopy, DICP, CAS.

#### Appendix A. Supporting information

Supplementary data associated with this article can be found in the online version at [doi:10.1016/j.apcatb.2023.122476](https://doi.org/10.1016/j.apcatb.2023.122476).

#### References

- [1] M.D. Porosoff, B.H. Yan, J.G.G. Chen, Catalytic reduction of CO<sub>2</sub> by H<sub>2</sub> for synthesis of CO, methanol and hydrocarbons: challenges and opportunities, *Energy Environ. Sci.* 9 (2016) 62–73.
- [2] J. Wei, R. Yao, Y. Han, Q. Ge, J. Sun, Towards the development of the emerging process of CO<sub>2</sub> heterogeneous hydrogenation into high-value unsaturated heavy hydrocarbons, *Chem. Soc. Rev.* 50 (2021) 10764–10805.
- [3] D. Wang, Z.H. Xie, M.D. Porosoff, J.G.G. Chen, Recent advances in carbon dioxide hydrogenation to produce olefins and aromatics, *Chem* 7 (2021) 2277–2311.
- [4] T.J. Wu, J. Lin, Y. Cheng, J. Tian, S.W. Wang, S.H. Xie, Y. Pei, S.R. Yan, M.H. Qiao, H.L. Xu, B.N. Zong, Porous graphene-confined Fe-K as highly efficient catalyst for CO<sub>2</sub> direct hydrogenation to light olefins, *ACS Appl. Mater. Interfaces* 10 (2018) 23439–23443.
- [5] A. Ramirez, L. Gevers, A. Bavykina, S. Ould-Chikh, J. Gascon, Metal organic framework-derived iron catalysts for the direct hydrogenation of CO<sub>2</sub> to short chain olefins, *ACS Catal.* 8 (2018) 9174–9182.
- [6] J. Zhu, P. Wang, X.B. Zhang, G.H. Zhang, R.T. Li, W.H. Li, T.P. Senftle, W. Liu, J. Y. Wang, Y.L. Wang, A.F. Zhang, Q. Fu, C.S. Song, X.W. Guo, Dynamic structural evolution of iron catalysts involving competitive oxidation and carburization during CO<sub>2</sub> hydrogenation, *Sci. Adv.* 8 (2022) eabm3629.
- [7] J. Wei, Q.J. Ge, R.W. Yao, Z.Y. Wen, C.Y. Fang, L.S. Guo, H.Y. Xu, J. Sun, Directly converting CO<sub>2</sub> into a gasoline fuel, *Nat. Commun.* 8 (2017) 15174.
- [8] C. Yang, B. Zhao, R. Gao, S.Y. Yao, P. Zhai, S.W. Li, J. Yu, Y.L. Hou, D. Ma, Construction of synergistic Fe<sub>5</sub>C<sub>2</sub>/Co heterostructured nanoparticles as an enhanced low temperature Fischer-Tropsch synthesis catalyst, *ACS Catal.* 7 (2017) 5661–5667.
- [9] W.H. Li, X.W. Nie, X. Jiang, A.F. Zhang, F.S. Ding, M. Liu, Z.M. Liu, X.W. Guo, C. S. Song, ZrO<sub>2</sub> support imparts superior activity and stability of Co catalysts for CO<sub>2</sub> methanation, *Appl. Catal. B-Environ.* 220 (2018) 397–408.
- [10] W.H. Li, X.W. Nie, H. Yang, X. Wang, F. Polo-Garzon, Z.L. Wu, J. Zhu, J.Y. Wang, Y. Liu, C. Shi, C.S. Song, X.W. Guo, Crystallographic dependence of CO<sub>2</sub> hydrogenation pathways over HCP-Co and FCC-Co catalysts, *Appl. Catal. B-Environ.* 315 (2022), 121529.
- [11] M.R. Wang, G.H. Zhang, J. Zhu, W.H. Li, J.Y. Wang, K. Bian, Y. Liu, F.S. Ding, C. S. Song, X.W. Guo, Unraveling the tunable selectivity on cobalt oxide and metallic cobalt sites for CO<sub>2</sub> hydrogenation, *Chem. Eng. J.* 446 (2022), 137217.
- [12] L. Guo, X. Gao, W. Gao, H. Wu, X. Wang, S. Sun, Y. Wei, Y. Kugue, X. Guo, J. Sun, N. Tsubaki, High-yield production of liquid fuels in CO<sub>2</sub> hydrogenation on a zeolite-free Fe-based catalyst, *Chem. Sci.*, (2022).
- [13] M.K. Gnanamani, G. Jacobs, H.H. Hamdeh, W.D. Shafer, F. Liu, S.D. Hopps, G. A. Thomas, B.H. Davis, Hydrogenation of carbon dioxide over Co-Fe bimetallic catalysts, *ACS Catal.* 6 (2016) 913–927.
- [14] H. Yang, Y. Dang, X. Cui, X. Bu, J. Li, S. Li, Y. Sun, P. Gao, Selective synthesis of olefins via CO<sub>2</sub> hydrogenation over transition-metal-doped iron-based catalysts, *Appl. Catal. B Environ.* 321 (2023), 122050.
- [15] F. Song, X. Yong, X. Wu, W. Zhang, Q. Ma, T. Zhao, M. Tan, Z. Guo, H. Zhao, G. Yang, N. Tsubaki, Y. Tan, FeMn@HZSM-5 capsule catalyst for light olefins direct synthesis via Fischer-Tropsch synthesis: studies on depressing the CO<sub>2</sub> formation, *Appl. Catal. B Environ.* 300 (2022), 120713.
- [16] A.S.M. Ismail, M. Casavola, B.Y. Liu, A. Gloter, T.W. van Deelen, M. Versluijs, J. D. Meeldijk, O. Stephan, K.P. de Jong, F.M.F. de Groot, Atomic-scale investigation of the structural and electronic properties of cobalt-iron bimetallic Fischer-Tropsch catalysts, *ACS Catal.* 9 (2019) 7998–8011.
- [17] Q. Yang, V.A. Kondratenko, S.A. Petrov, D.E. Doronkin, E. Saraçi, H. Lund, A. Arinchtin, R. Kraehnert, A.S. Skrypnik, A.A. Matvienko, E.V. Kondratenko, Identifying performance descriptors in CO<sub>2</sub> hydrogenation over iron-based catalysts promoted with alkali metals, *Angew. Chem. Int. Ed.* 61 (2022) e202116517.
- [18] R. Sathawong, N. Koizumi, C.S. Song, P. Prasassarakich, Light olefin synthesis from CO<sub>2</sub> hydrogenation over K-promoted Fe-Co bimetallic catalysts, *Catal. Today* 251 (2015) 34–40.
- [19] M.K. Gnanamani, H.H. Hamdeh, G. Jacobs, W.D. Shafer, S.D. Hopps, G.A. Thomas, B.H. Davis, Hydrogenation of carbon dioxide over K-promoted FeCo bimetallic catalysts prepared from mixed metal oxalates, *ChemCatChem* 9 (2017) 1303–1312.
- [20] Q. Xu, X. Xu, G. Fan, L. Yang, F. Li, Unveiling the roles of Fe-Co interactions over ternary spinel-type ZnCo<sub>x</sub>Fe<sub>2-x</sub>O<sub>4</sub> catalysts for highly efficient CO<sub>2</sub> hydrogenation to produce light olefins, *J. Catal.* 400 (2021) 355–366.
- [21] F. Yuan, G.H. Zhang, J. Zhu, F.S. Ding, A.F. Zhang, C.S. Song, X.W. Guo, Boosting light olefin selectivity in CO<sub>2</sub> hydrogenation by adding Co to Fe catalysts within close proximity, *Catal. Today* 371 (2021) 142–149.
- [22] G.B. Chen, R. Gao, Y.F. Zhao, Z.H. Li, G.L.N. Waterhouse, R. Shi, J.Q. Zhao, M. T. Zhang, L. Shang, G.Y. Sheng, X.P. Zhang, X.D. Wen, L.Z. Wu, C.H. Tung, T. R. Zhang, Alumina-supported CoFe alloy catalysts derived from layered-double-hydroxide nanosheets for efficient photothermal CO<sub>2</sub> hydrogenation to hydrocarbons, *Adv. Mater.* 30 (2018) 1704663.
- [23] S. Lee, M. Govindan, D. Kim, CoFe-based layered double hydroxide for high removal capacity of hydrogen sulfide under high humid gas stream, *Chem. Eng. J.* 416 (2021), 127918.
- [24] L. Zhang, Y.R. Dang, X.H. Zhou, P. Gao, A.P. van Bavel, H. Wang, S.G. Li, L. Shi, Y. Yang, E.I. Vovk, Y.H. Gao, Y.H. Sun, Direct conversion of CO<sub>2</sub> to a jet fuel over CoFe alloy catalysts, *Innovation* 2 (2021), 100170.
- [25] J.Q. Zhao, R. Shi, G.L.N. Waterhouse, T.R. Zhang, Selective photothermal CO<sub>2</sub> reduction to CO, CH<sub>4</sub>, alkanes, alkenes over bimetallic alloy catalysts derived from layered double hydroxide nanosheets, *Nano Energy* 102 (2022), 107650.



- [26] S.M. Hwang, S.J. Han, H.G. Park, H. Lee, K. An, K.W. Jun, S.K. Kim, Atomically alloyed Fe-Co catalyst derived from a N-Coordinated Co single-atom structure for CO<sub>2</sub> hydrogenation, *ACS Catal.* 11 (2021) 2267–2278.
- [27] D. Long, X.Y. Li, Z.F. Yin, S.Y. Fan, P.L. Wang, F.Q. Xu, L.H. Wei, M.O. Tade, S. M. Liu, Novel Co<sub>3</sub>O<sub>4</sub>@CoFe<sub>2</sub>O<sub>4</sub> double-shelled nanoboxes derived from Metal-Organic Framework for CO<sub>2</sub> Reduct., *J. Alloy. Compd.* 854 (2021), 156942.
- [28] M. Athariboroujeny, A. Raub, V. Iablokov, S. Chenakin, L. Kovarik, N. Kruse, Competing mechanisms in CO hydrogenation over Co-MnO<sub>x</sub> catalysts, *ACS Catal.* 9 (2019) 5603–5612.
- [29] K.Y. Kim, H. Lee, W.Y. Noh, J. Shin, S.J. Han, S.K. Kim, K. An, J.S. Lee, Cobalt ferrite nanoparticles to form a catalytic Co-Fe alloy carbide phase for selective CO<sub>2</sub> hydrogenation to light olefins, *ACS Catal.* 10 (2020) 8660–8671.
- [30] S. Li, P. Ren, C. Yang, X. Liu, Z. Yin, W. Li, H. Yang, J. Li, X. Wang, Y. Wang, R. Cao, L. Lin, S. Yao, X. Wen, D. Ma, Fe<sub>5</sub>C<sub>2</sub> nanoparticles as low-cost HER electrocatalyst: the importance of Co substitution, *Sci. Bull.* 63 (2018) 1358–1363.
- [31] G.P. Wu, J. Wang, W. Ding, Y. Nie, L. Li, X.Q. Qi, S.G. Chen, Z.D. Wei, A strategy to promote the electrocatalytic activity of spinels for oxygen reduction by structure reversal, *Angew. Chem. Int. Ed.* 55 (2016) 1340–1344.
- [32] M. Ding, Synthesis and characterization of alpha-Fe<sub>2</sub>O<sub>3</sub> nanocubes via hydrothermal method, *Asian J. Chem.* 26 (2014) 1808–1810.
- [33] J.I. Oregre, J. Wei, Y. Han, M. Yang, X.T. Sun, J.X. Zhang, C.C. Amoo, Q.J. Ge, J. Sun, Highly stable Sr and Na co-decorated Fe catalyst for high-valued olefin synthesis from CO<sub>2</sub> hydrogenation, *Appl. Catal. B-Environ.* 316 (2022), 121640.
- [34] W.F. Tu, C. Sun, Z.Z. Zhang, W.Q. Liu, H.S. Malhi, W. Ma, M.H. Zhu, Y.F. Han, Chemical and structural properties of Na decorated Fe<sub>5</sub>C<sub>2</sub>-ZnO catalysts during hydrogenation of CO<sub>2</sub> to linear alpha-olefins, *Appl. Catal. B-Environ.* 298 (2021), 120567.
- [35] R. Ning, J. Tian, A.M. Asiri, A.H. Qusti, A.O. Al-Youbi, X. Sun, Spinel CuCo<sub>2</sub>O<sub>4</sub> nanoparticles supported on N-doped reduced graphene oxide: A highly active and stable hybrid electrocatalyst for the oxygen reduction reaction, *Langmuir* 29 (2013) 13146–13151.
- [36] Z. Zeng, Z. Li, L. Kang, X. Han, Z. Qi, S. Guo, J. Wang, A. Rykov, J. Lv, Y. Wang, X. Ma, A monodisperse ε'-(Co<sub>x</sub>Fe<sub>1-x</sub>)<sub>2</sub>C bimetallic carbide catalyst for direct conversion of syngas to higher alcohols, *ACS Catal.* (2022) 6016–6028.
- [37] Y.R. Hao, H. Xue, L. Lv, J. Sun, N.K. Guo, T.S. Song, H.L. Dong, J.W. Zhang, Q. Wang, Unraveling the synergistic effect of defects and interfacial electronic structure modulation of pealike CoFe@Fe<sub>3</sub>N to achieve superior oxygen reduction performance, *Appl. Catal. B-Environ.* 295 (2021), 120314.
- [38] T.F. Li, Y.J. Lv, J.H. Su, Y. Wang, Q. Yang, Y.W. Zhang, J.C. Zhou, L. Xu, D.M. Sun, Y.W. Tang, Anchoring CoFe<sub>2</sub>O<sub>4</sub> nanoparticles on N-doped carbon nanofibers for high-performance oxygen evolution reaction, *Adv. Sci.* 4 (2017) 1700226.
- [39] X. Chen, B. Liu, C. Zhong, Z. Liu, J. Liu, L. Ma, Y.D. Deng, X.P. Han, T.P. Wu, W. B. Hu, J. Lu, Ultrathin Co<sub>3</sub>O<sub>4</sub> layers with large contact area on carbon fibers as high-performance electrode for flexible Zinc-air battery integrated with flexible display, *Adv. Energy Mater.* 7 (2017) 1700779.
- [40] J. Choi, D. Kim, S.J. Hong, X.D. Zhang, H. Hong, H. Chun, B. Han, L.Y.S. Lee, Y. Piao, Tuning the electronic structure and inverse degree of inverse spinel ferrites by integrating samarium orthoferrite for efficient water oxidation, *Appl. Catal. B-Environ.* 315 (2022), 121504.
- [41] S. Storck, H. Bretinger, W.F. Maier, Characterization of micro- and mesoporous solids by physisorption methods and pore-size analysis, *Appl. Catal. A-Gen.* 174 (1998) 137–146.
- [42] Y. Xiang, Y. Zhu, J. Lu, C.Z. Zhu, M.Y. Zhu, Q.Q. Xie, T.H. Chen, Co<sub>3</sub>O<sub>4</sub>/alpha-Fe<sub>2</sub>O<sub>3</sub> catalyzed oxidative degradation of gaseous benzene: preparation, characterization and its catalytic properties, *Solid State Sci.* 93 (2019) 79–86.
- [43] W.K. Jozwiak, E. Kaczmarek, T.P. Maniecki, W. Ignaczak, W. Maniukiewicz, Reduction behavior of iron oxides in hydrogen and carbon monoxide atmospheres, *Appl. Catal. A-Gen.* 326 (2007) 17–27.
- [44] J. Xu, J. Wei, J. Zhang, R. Yao, Q. Ge, Q. Ma, J. Sun, Highly selective production of long-chain aldehydes, ketones or alcohols via syngas at a mild condition, *Appl. Catal., B* 307 (2022), 121155.
- [45] H.Y. Lin, Y.W. Chen, The mechanism of reduction of cobalt by hydrogen, *Mater. Chem. Phys.* 85 (2004) 171–175.
- [46] J. Wei, R. Yao, Q. Ge, D. Xu, C. Fang, J. Zhang, H. Xu, J. Sun, Precisely regulating Brønsted acid sites to promote the synthesis of light aromatics via CO<sub>2</sub> hydrogenation, *Appl. Catal. B Environ.* 283 (2021), 119648.
- [47] X.N. Li, K.Y. Zhu, J.F. Pang, M. Tian, J.Y. Liu, A.I. Rykov, M.Y. Zheng, X.D. Wang, X.F. Zhu, Y.Q. Huang, B. Liu, J.H. Wang, W.S. Yang, T. Zhang, Unique role of Mössbauer spectroscopy in assessing structural features of heterogeneous catalysts, *Appl. Catal. B-Environ.* 224 (2018) 518–532.
- [48] Y. Zeng, X. Li, J. Wang, M.T. Sougrati, Y. Huang, T. Zhang, B. Liu, In situ/operando Mössbauer spectroscopy for probing heterogeneous catalysis, *Chem. Catal.* 1 (2021) 1215–1233.
- [49] X.W. Liu, S. Zhao, Y. Meng, Q. Peng, A.K. Dearden, C.F. Huo, Y. Yang, Y.W. Li, X. D. Wen, Mössbauer spectroscopy of iron carbides: from prediction to experimental confirmation, *Sci. Rep.* 6 (2016) 26184.
- [50] F.H. Meng, Z. Li, F.K. Ji, M.H. Li, Effect of ZrO<sub>2</sub> on catalyst structure and catalytic methanation performance over Ni-based catalyst in slurry-bed reactor, *Int. J. Hydrog. Energy* 40 (2015) 8833–8843.
- [51] J. Xu, C.R. Bartholomew, Temperature-programmed hydrogenation (TPH) and in situ Mössbauer spectroscopy studies of carbonaceous species on silica-supported iron Fischer-Tropsch catalysts, *J. Phys. Chem. B* 109 (2005) 2392–2403.
- [52] K.F. Tan, J. Xu, J. Chang, A. Borgna, M. Saeys, Carbon deposition on Co catalysts during Fischer-Tropsch synthesis: a computational and experimental study, *J. Catal.* 274 (2010) 121–129.
- [53] D. Pena, A. Cognigni, T. Neumayer, W. van Beek, D.S. Jones, M. Quijada, M. Ronning, Identification of carbon species on iron-based catalysts during Fischer-Tropsch synthesis, *Appl. Catal. A-Gen.* 554 (2018) 10–23.
- [54] M.J. Xu, X.L. Liu, G.Y. Song, Y.Y. Cai, B.F. Shi, Y.T. Liu, X.X. Ding, Z.X. Yang, P. F. Tian, C.X. Cao, J. Xu, Regulating iron species compositions by Fe-Al interaction in CO<sub>2</sub> hydrogenation, *J. Catal.* 413 (2022) 331–341.
- [55] A. Rodriguez-Gomez, J.P. Holgado, A. Caballero, Cobalt carbide identified as catalytic site for the dehydrogenation of ethanol to acetaldehyde, *ACS Catal.* 7 (2017) 5243–5247.
- [56] F. Wang, S. He, H. Chen, B. Wang, L. Zheng, M. Wei, D.G. Evans, X. Duan, Active site dependent reaction mechanism over Ru/CeO<sub>2</sub> catalyst toward CO<sub>2</sub> methanation, *JACS* 138 (2016) 6298–6305.
- [57] R. Yao, J. Wei, Q. Ge, J. Xu, Y. Han, Q. Ma, H. Xu, J. Sun, Monometallic iron catalysts with synergistic Na and S for higher alcohols synthesis via CO<sub>2</sub> hydrogenation, *Appl. Catal. B-Environ.* 298 (2021), 120556.
- [58] M.K. Khan, P. Butolia, H. Jo, M. Irshad, D. Han, K.W. Nam, J. Kim, Selective conversion of carbon dioxide into liquid hydrocarbons and long-chain alpha-olefins over Fe-amorphous AlO<sub>x</sub> bifunctional catalysts, *ACS Catal.* 10 (2020) 10325–10338.
- [59] P. Gao, L.N. Zhang, S.G. Li, Z.X. Zhou, Y.H. Sun, Novel heterogeneous catalysts for CO<sub>2</sub> hydrogenation to liquid fuels, *ACS Cent. Sci.* 6 (2020) 1657–1670.
- [60] Y.F. Zhu, X.L. Pan, F. Jiao, J. Li, J.H. Yang, M.Z. Ding, Y. Han, Z. Liu, X.H. Bao, Role of manganese oxide in syngas conversion to light olefins, *ACS Catal.* 7 (2017) 2800–2804.
- [61] J.Q. Zhao, X.D. Guo, R. Shi, G.I.N. Waterhouse, X.R. Zhang, Q. Dai, T.R. Zhang, NiFe nanoalloys derived from layered double hydroxides for photothermal synergistic reforming of CH<sub>4</sub> with CO<sub>2</sub>, *Adv. Funct. Mater.* 32 (2022).